TECHNISCHE
UNIVERSITÄT
MÜNCHEN

NAT
TUM School of
Natural Sciences

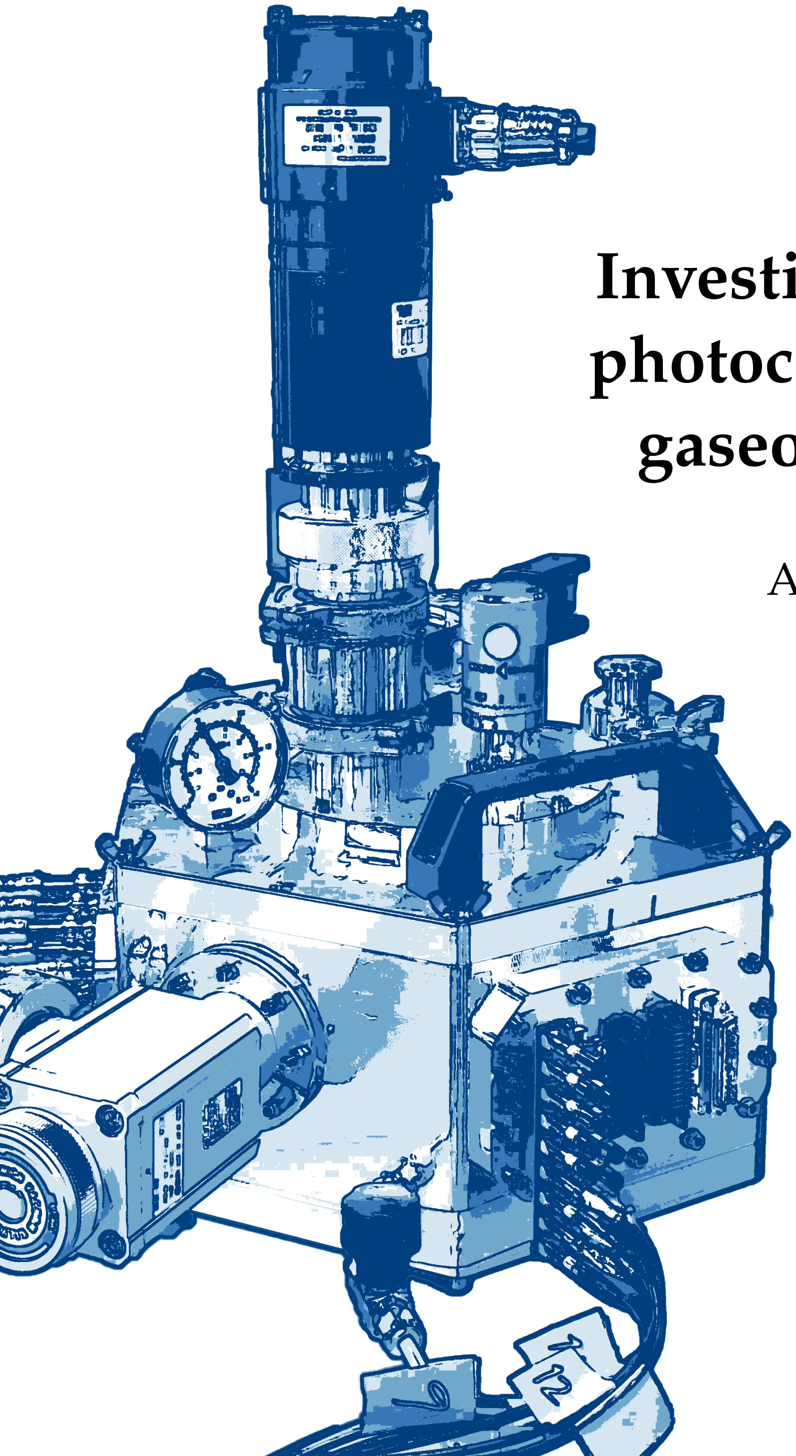

Bachelor's Thesis

Investigation of DLC as a photocathode material for gaseous light detectors

Anıl Berkay Adıgüzel

TECHNISCHE UNIVERSITÄT MÜNCHEN

TUM School of
Natural Sciences

Investigation of DLC as a photocathode material for gaseous light detectors

Untersuchung von DLC als Photokathodenmaterial für gasgefüllte Lichtdetektoren

Bachelor's Thesis

Author: Anıl Berkay Adıgüzel
Examiner: Prof. Dr. Laura Fabbietti
Supervisor: Berkin Ulukutlu
Date: January 9, 2024

I confirm that the results presented in this bachelor's thesis are my own work, and I have documented all sources and materials used.

Ich versichere, dass ich diese Bachelorarbeit selbstständig verfasst und nur die angegebenen Quellen und Hilfsmittel verwendet habe.

Munich, January 9, 2024 Anıl Berkay Adıgüzel

Abstract

Photon detection plays a crucial role in fundamental physics, serving as the cornerstone for numerous experiments and groundbreaking discoveries. The detection and analysis of photons are pivotal within this intricate field dedicated to uncovering the universe's fundamental constituents and their interactions. Due to their excellent detection capabilities, detector technologies such as silicon photomultipliers and photomultiplier tubes are most frequently utilized. However, these methods can be costly for large-scale measurement experiments. Micro-pattern-gas-detector (MPGD) based photon detectors promise to be a good alternative due to their simplicity of manufacturing at large scales. Due to this, numerous studies have been conducted over the years with the goal of creating MPGD photodetectors, with a particular emphasis on examining possible photocathode materials. In this thesis, diamond-like carbon is investigated using two different measurement modes: transmissive mode and reflective mode. In the reflective mode, copper plates coated with DLC were utilized to assess the Quantum Efficiency (QE) of DLC. Surprisingly, the QE values for copper with and without DLC coating proved identical, indicating the negligible impact of DLC in this measurement configuration. In the transmissive mode, an Ar-CH4 (90-10) gas mixture, a multi-pad anode with 64 individual pads, and two THGEMs are used. A DLC-coated MgF_2 window is used as the sample in transmissive mode. A QE value of $5.93(371) \times 10^{-5}$ is reported.

1 Introduction

Photon detection plays a crucial role in fundamental physics, serving as the cornerstone for numerous experiments and groundbreaking discoveries. Within this intricate field dedicated to uncovering the universe's fundamental constituents and their interactions, the detection and analysis of photons are pivotal. As elementary particles of light, photons are not only carriers of the electromagnetic force but also bear vital information about particle interactions. They are instrumental in particle identification, enabling the understanding of the particles involved in various interactions, and play a critical role in energy measurement by revealing the energy levels of particles through their detection.

Countless experiments utilize photodetectors; for example, the Super-Kamiokande uses 11146 individual photodetectors to detect Cherenkov radiation produced by neutrino interactions [1]. Super-Kamiokande provided crucial data that allowed scientists to deepen their understanding of neutrino oscillations the nature of atmospheric, solar, and astrophysical neutrinos [1]. Similarly, photodetectors are used in cosmic-ray detection. The Pierre Auger Observatory studies the highest-energy particles produced by cosmic-ray particles [2]. By detecting and analyzing these particles, the Pierre Auger Observatory aims to expand the comprehension of their origin and existence. Photodetectors are also used in experiments related to dark matter searches, such as the XENON experiment. The XENON experiment is a collaborative scientific effort aimed at the direct detection of dark matter, which is one of the most significant mysteries in modern astrophysics and cosmology. XENON experiment employs photosensors to detect faint scintillation signals produced by potential dark matter candidates such as weakly interacting massive particles [3].

Especially in particle and nuclear physics, the demand for advanced large-scale photon detectors resonates across diverse experiments, whether in colliders, fixed-target setups, or low-energy nuclear physics. These detectors, pivotal for a myriad of applications, play a crucial role in capturing elusive particles and deciphering the intricacies of fundamental interactions. Notably, the necessity for reliable, cost-effective, and scalable photon detectors becomes even more pronounced in experiments such as those involving RICH detectors, which are used for particle identification at the LHCb experiment [4]. The overarching goal of our measurements aligns with the imperative to contribute to the development of large-scale, economical photon detectors—a pursuit with far-reaching implications for advancing the frontiers of experimental physics.

1.1 Types of Photodetectors

In order to detect a photon, a photodetector converts incident photons into an electrical signal. Thus making it possible to measure and analyze the properties of the light. To achieve this goal, a range of photon detectors has been developed, each with distinct advantages and disadvantages. These detectors include Photomultiplier Tubes (PMTs), which are efficient and radiation hard but expensive; Avalanche Photodiodes (APDs), offering high sensitivity and speed but susceptible to noise and temperature fluctuations; and Silicon Photomultipliers (SiPMs), which combine sensitivity, compactness, and low noise, thus emerging as a promising choice for various experiments- yet they are not radiation hard. Additionally, photodetector arrays provide spatial information, albeit potentially with lower sensitivity. It's crucial to highlight that our discussion covers only certain aspects of these detectors, offering a focused viewpoint rather than a thorough analysis. The selection of the appropriate photon detector for a given experiment hinges on factors like sensitivity, dynamic range, response time, scalability, rate capabilities, and cost, necessitating careful consideration to ensure it aligns with the specific requirements and conditions of the application.

1.1.1 Photomultiplier Tubes

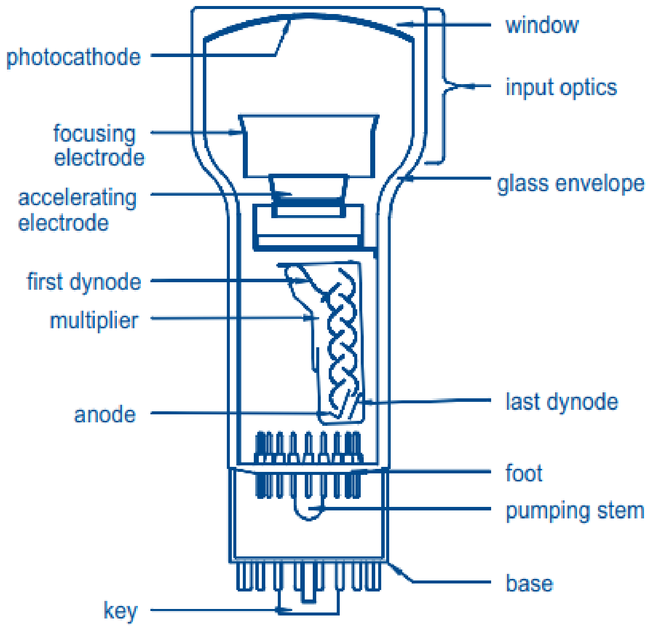

Figure 1.1: Structure of photomultiplier tube with labeled components. Taken from [5]

A PMT is a non-thermionic vacuum tube, typically composed of glass, that transforms light into an electric current that can be measured. PMTs are versatile and sensitive detectors that amplify incoming photons using a cascading chain of electron multiplication [6]. It consists of a photosensitive cathode at one end, which absorbs incoming photons and emits electrons through the photoelectric effect. These emitted electrons are then accelerated and focused by a series of dynodes, which are metal electrodes with increasingly positive voltages. As electrons strike each dynode, they undergo multiplication through secondary emission, resulting in a cascade effect that significantly amplifies the initial photocurrent. Finally, an anode collects the multiplied electrons, generating an output signal proportional to the incident light intensity. PMTs are often housed in a vacuum-sealed glass or metal envelope to prevent interference from external factors and maintain their high sensitivity to even very low levels of light. Figure 1.1 shows the structure of a typical PMT.

PMTs have an ultra-fast response and low noise with high gain, which makes them highly efficient at detecting low-intensity light [7]. This makes PMTs suitable for applications such as scintillation counters and Cherenkov detectors. But in terms of size, cost, and efficiency, PMTs are getting close to their limits [6]. In contrast, multi-anode PMTs(MaPMT) offer a solution as they can be stacked into groups called elementary cells to cover a large area [8] thanks to their compact structure. Despite their advantages, it's essential to note that PMTs and MaPMTs operate in a vacuum, presenting challenges that contribute to increased production difficulty and cost.

1.1.2 Avalanche Photodiodes

APDs are semiconductor devices used for high-sensitivity detection of photons, particularly in applications like the detection of weak light signals, such as those produced in high-energy particle interactions. Their structure, as shown in Figure 1.2, consists of a p-n junction, where a heavily doped p-type region and a moderately doped n-type region are connected.

An APD exploits the photoelectric effect to convert light into electricity. From a functional standpoint, they can be regarded as the semiconductor analog of PMTs. The working principle of APDs is based on the avalanche multiplication effect [10]. When a photon with sufficient energy strikes the APD's absorption region, it transfers its energy to electrons within the material, generating an electron-hole pair through the photoelectric effect [6]. Due to the high electric field applied across the p-n junction (typically achieved by biasing the APD in the reverse-biased mode), the generated electron undergoes impact ionization [10]. This means that the electron gains enough energy from the electric field to collide with other atoms in the semiconductor material, creating additional electron-hole pairs in a chain reaction. This avalanche multiplication results in a significant increase in the number of charge carriers, leading to a much higher photocurrent than the initial photon would produce alone. This amplified current is then collected as the output signal.

However, APDs are prone to excess noise [11], primarily due to the stochastic nature of the avalanche process during impact ionization. This noise can limit their performance, particularly in low-light conditions. They require a relatively high bias voltage to maintain the electric field needed for impact ionization. Managing these high voltages can be challenging and requires specialized power supplies and voltage regulation. Furthermore, APDs are sensitive to temperature variations; changes in the temperature can affect the breakdown voltage and multiplication factor, leading to variations in their performance. While APDs are smaller than some alternative detectors like Photomultiplier Tubes (PMTs), they are still relatively bulky, which can limit their integration into compact and portable devices.

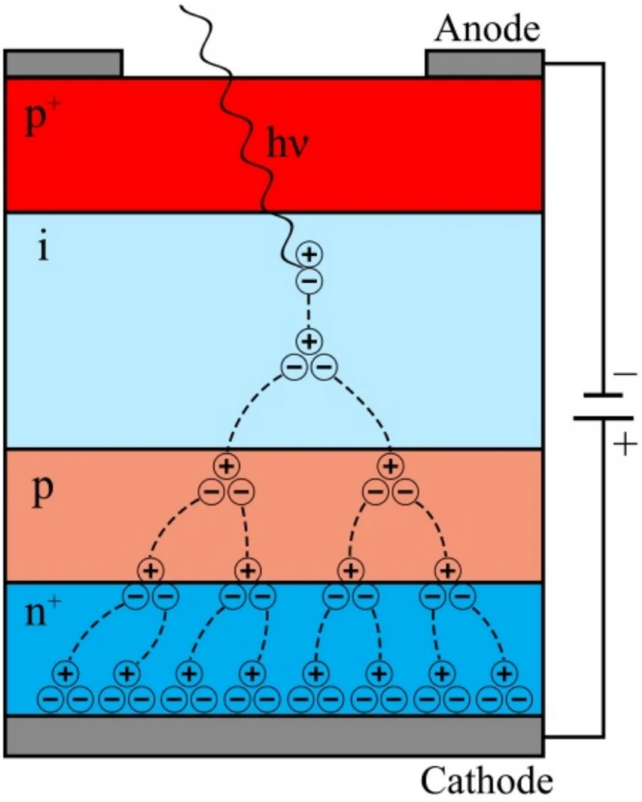

Figure 1.2: Cross-section of an avalanche photodiode and its operating principle. Taken from [9]

1.1.3 Silicon Photomultipliers

SiPMs are advanced solid-state detectors that combine the advantages of APDs with improved noise characteristics [6]. They are designed to detect low levels of light with high sensitivity and fast response times, offer high photon detection efficiency, and have a wide dynamic range. SiPMs are increasingly popular in particle physics experiments.

A SiPM consists of a matrix of thousands to millions of tiny individual photodiode pixels, all connected in parallel. Each pixel is a miniature photodiode with a silicon avalanche diode, known as a single photon avalanche diode (SPAD), at its core. The pixels are closely packed together on a low resistivity silicon strate, and each pixel is connected to a quenching resistor and a shared readout circuit. The entire SiPM is typically sealed in a light-tight package [12]. The generic structure of the SiPM cell is presented in Figure 1.3.

When a photon strikes the silicon material within a pixel, it generates electron-hole pairs through the photoelectric effect. If the photon's energy is sufficient, these charge carriers can trigger an avalanche breakdown in the SPAD. This avalanche process causes a rapid increase in the number of charge carriers within the pixel, resulting in a detectable electrical signal. SiPMs are designed to operate in Geiger mode, where each SPAD either entirely breaks down or remains quenched. When a SPAD breaks down, it creates a distinct output pulse, indicating

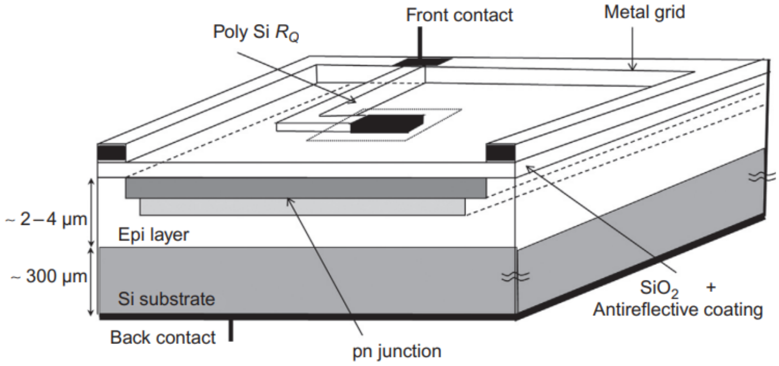

Figure 1.3: The generic structure of SiPM cell. Taken from [12]

the detection of a photon. The quenching resistor and shared readout circuit help reset the SPADs quickly after each breakdown event, allowing the SiPM to detect successive photons rapidly. The output of a SiPM is a series of discrete electrical pulses, and the number and timing of these pulses correspond to the number and arrival times of detected photons.

Compared to conventional PMTs, the photoelectron gain in SiPMs is typically more deterministic, resulting in low or even negligible excess noise factor [6]. Despite that, SiPMs have limitations, including dark counts causing noise, afterpulsing affecting timing, limited dynamic range leading to saturation. Moreover, the SiPMs are prone to damage from radiation, showing a decrease in gain up to 19% [13]. Furthermore, SiPMs are sensitive to temperature [14]. They may require ambient cooling, while a PMT used in the same application may not, increasing complexity and cost. Similarly, obtaining large active areas may be difficult due to higher dark counts per area than in PMTs.

1.2 Gaseous Particle Detectors

Gaseous particle detectors are indispensable tools in nuclear and particle physics, as well as in various radiation detection and measurement applications. These devices allow scientists to identify, quantify, and characterize ionizing radiation from various sources, such as radioactive materials or high-energy particle interactions. Their design and operation are grounded in ionization and charge collection principles within a gaseous medium.

At their core, gaseous particle detectors utilize the interactions between ionizing radiation and the atoms or molecules of the gas enclosed within the detector volume. As particles traverse the gas volume, they transfer energy to the gas atoms or molecules, creating electron-ion pairs. It should be noted that there are several mechanisms of energy loss. Nevertheless, in the scope of this thesis, ionizing energy loss is the most relevant mechanism. The charged particles created within the gas can be collected, amplified, and analyzed to gain information about the incoming particle.

These detectors come in various designs and configurations, each tailored to the specific requirements of the experiment. Some of the commonly used types are parallel-plate chambers, wire-counters, multi-wire proportional chambers, drift chambers, and time projection chambers. Selecting a particular gaseous particle detector hinges on evaluating several pivotal factors. The energy range of the particles under investigation significantly influences the choice, as different detectors exhibit varying sensitivities across energy spectra. Sensitivity requirements are also crucial, with some experiments necessitating heightened sensitivity to detect even low radiation levels. In contrast, others prioritize a broader dynamic range or the capacity to handle high particle fluxes. Moreover, the necessity for precise spatial resolution, especially in contexts where the accurate localization of particle interactions is imperative, influences the selection of detectors with superior spatial resolution.

1.2.1 Working Principle of Gaseous Detectors

Gaseous ionization detectors are radiation detection tools used to determine the existence of ionizing particles by employing the ionizing effects of radiation using the gas within the detector as a working medium. The process begins with releasing one or more ion–electron pairs in gas as a particle traverses the detector volume. The number of pairs, as well as the distribution, is dependent on the nature of the radiation and the properties of the chosen gas. Furthermore, if the primary electrons possess sufficient energy, they can further ionize the gas molecules, leading to a cascade of secondary interactions that increase the number of released electrons. This phenomenon continues until the available energy loss is dissipated and the various yields reach thermal equilibrium [15].

Once released into the gas, electrons, and ions may neutralize by colliding with the detector or by recombining with one another. When an external electric field is applied, ion-electron pairs separate and migrate towards the electrodes of the counter. Depending on the primary ionization density and the gas, the required field strength for separation is typically a few tens of $\mathrm{V\,cm^{-1}}$ in argon at standard pressure and temperature [15]. Once separated, electrons and ions diffuse thermally within the gas volume, moving randomly due to molecular collisions, with a constant velocity in the field's direction known as drift velocity. Finally, the electrons and ions drift into the electrodes of the detectors under the influence of the electric field, which allows the detection via current measurement [16].

Energy loss within the gas

Various macroscopic mechanisms can be used to convert energy deposited into the medium into a detectable signal. These mechanisms include scintillation in fluorescent materials, condensation of droplets in saturated vapors, ionization, and emission of transition radiation.

The ionization component of energy loss is the main focus of this thesis's considerations. This is because, in gases, other processes such as excitation, scintillation, or luminescence often yield low signal strengths, making them unsuitable for practical detection. Furthermore, some of these processes generate photons, and to effectively detect them, one may need photon detection techniques, which is ultimately the main point of this investigation. When charged particles traverse a medium, they interact with the atomic electron clouds, leading to excitation or ionization of the atoms [17]. These interactions involve electromagnetic forces between the charged particles and the surrounding medium, resulting in the maximum energy dissipation within the medium [15]. The energy loss due to ionization is calculated using the Bethe-Bloch formula, which reads as follows:

$$-\left\langle \frac{dE}{dx} \right\rangle = \frac{4\pi}{m_e c^2} \cdot \frac{nz^2}{\beta^2} \cdot \left(\frac{e^2}{4\pi\varepsilon_0} \right)^2 \cdot \left[\ln \left(\frac{2m_e c^2 \beta^2}{I \cdot (1-\beta^2)} \right) - \beta^2 \right] \tag{1.1}$$

where $\beta = v/c$ is the speed of the particle, ze the charge of the particle, n the electron density and I the average excitation potential of the atoms[17].

Electrons and photons created by the primary interaction can interact with the medium again, causing further excitation and ionization. Especially in composite materials, these secondary mechanisms contribute to the overall photon and electron yield [15].

Ions and electrons released in gas by ionization quickly lose their energy in multiple collisions with the surrounding particles and reach thermal equilibrium with the medium [15].

In the absence of external fields and inelastic collision, ions and electrons released in a gas behave like neutral molecules. Therefore, their properties can be described by the classic kinetic theory of gasses [15]. Maxwell-Boltzmann law states that the probability of a particle or a molecule having an energy ϵ at the absolute temperature is

$$P(\epsilon) = 2 \cdot \sqrt{\frac{\epsilon}{\pi (k_B T)^3}} \exp \frac{\epsilon}{k_B T} \tag{1.2}$$

where k_b, is the Boltzmann's constant. Therefore the average thermal energy, $\bar{\epsilon_T}$ is obtained by integrating over the distribution.

$$\bar{\epsilon_T} = k_b T$$

At normal conditions, $\bar{\epsilon_T} = 0.025\,\text{eV}$ see Figure 1.4.

One key distinction in the behavior of electrons and ions arises from the variance in their mass. While their energy distribution adheres to the same fundamental laws, the notably lower mass of electrons results in velocities that are orders of magnitude higher.

When an electric field is applied to the gas volume, a net movement of ions and electrons parallel to the field direction is observed. Electrons move in the direction opposite to the field whereas ions move in the direction of field vector. Because of their small mass, electrons can substantially increase their energy between collisions with the molecules of the gas. In a simple formulation, the electron drift velocity can be written as

$$w = k\frac{eE}{m}\tau \tag{1.3}$$

where τ is the mean time between collisions[18]. Nevertheless, this formulation is not encapsulating the whole physical phenomena because τ depends on the electric field [15], thus it more convenient for qualitative considerations. Furthermore, the mean time between collisions depends on the properties of the gas such as its composition and pressure. Electron drift velocity in argon-methane mixtures at NTP is shown in Figure 1.5, which is the only gas used in the scope of this thesis.

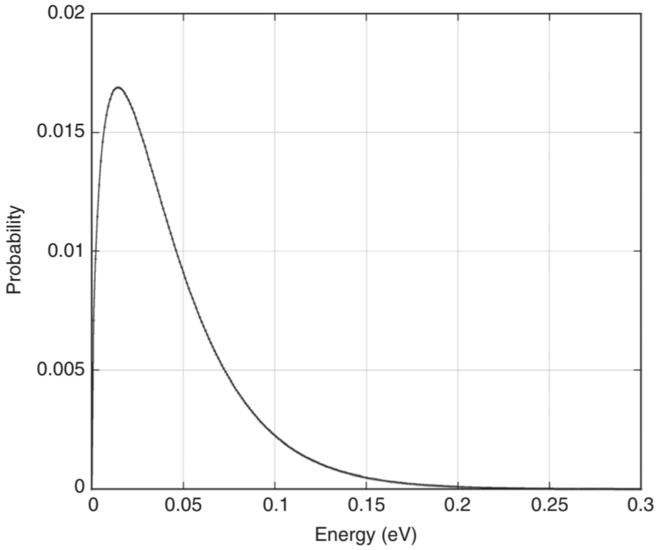

Figure 1.4: Energy distribution of molecules and particles at normal conditions. Taken from [15]

When an electric field on the order of a few $\mathrm{kV\,cm^{-1}}$ is applied, an increasing number of electrons can gain enough energy- in between two collisions- to cause inelastic phenomena; excitation of various kinds and ionizations.

At higher fields, the probability of ionization due to collisions increases and exceeds the probability of excitation [15]. As a result, more electron-ion pairs are generated while the primary electron continues its motion in the gas. The fundamental mechanism of signal amplification in gas proportional counters occurs when the mean free path for ionizing collisions is small in comparison to the thickness of the gas layer. This means that the electrons quickly obtain enough energy from the electric field to ionize further, which causes an electron-ion avalanche to grow quickly.

The mean free path for ionization, λ, refers to the average distance an electron has to travel before having an ionizing collision [19]. Therefore its inverse, $a = \lambda^{-1}$, is the average number of collisions per unit track length. This term is also known as the first Townsend coefficient and it is proportional to the ionization cross section [20]:

$$a = N\sigma_i \tag{1.4}$$

where N is the number of molecules per unit volume, and σ_i the ionization cross section. Therefore, it is also evident that the Townsend coefficient is proportional to the gas density and to the pressure.

Consider an electron, in a region of uniform electric field, one electron-ion pair will be produced after it moves a mean free path. Then the two electrons continue moving generating more electron-ion pairs and so on, which causes an exponential increase in the number of

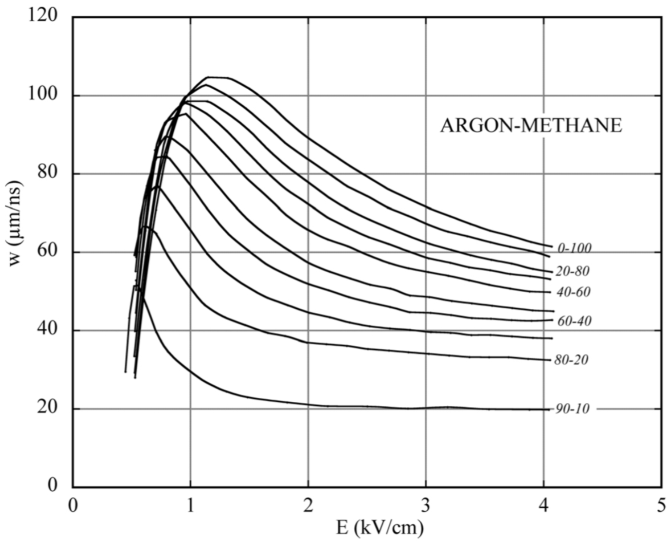

Figure 1.5: Electron drift velocity in argon-methane mixtures at NTP. Taken from [15]

electrons. Thus the number of electrons, n, is given as

$$n = n_0 e^{ax} \tag{1.5}$$

where x is the path length, and n_0 the initial number of electrons.

1.2.2 Gas Electron Multiplier

A type of gaseous particle detector is the gas electron multiplier (GEM) [15]. GEMs consist of a thin, perforated, insulating material sandwiched between two metal layers. A typical GEM is 50 µm thick and has holes with a pitch of 140 µm and a diameter of 70 µm [21]. These tiny holes or channels, are distributed across the insulating material.

When charged particles, such as electrons, traverse the gas-filled chamber, they ionize the gas, and these primary electrons mitigate towards the GEM. The primary electrons are then drawn through the holes in the insulating material by an applied electric field. As these electrons pass through the holes, they initiate a phenomenon known as electron avalanche multiplication. This process results in a significant amplification of the original signal.

One of the key advantages of GEM detectors is their ability to provide high spatial resolution and excellent sensitivity, making them valuable tools in various fields of research, including high-energy physics, nuclear physics, medical imaging, and more. They are particularly well-suited for experiments involving particle tracking and the precise measurement of ionizing radiation.

One variation of GEM detectors, known as thick GEM(THGEM) detectors, uses the same principle with thicker layers of metal and insulating [22, 23, 24]. THGEMs provide higher gain and allow for better position resolution. Furthermore, they are more resilient compared to their thinner counterparts. Ease of production is also a factor that needs to be taken into consideration when it comes to manufacturing a detector. GEMs are produced using a photolithography process and electrochemical etching of the metal and insulator layers, whereas THGEMs are made by milling holes in a PCB plate. A typical THGEM has a thickness of 0.2 - 1 mm, a hole diameter ranging between 0.2 - 1 mm, and a hole pitch of 0.5 - 1 mm [25]. The energy resolution of THGEM for 6 keV x-rays closely parallels that of GEM; however, there is a clear difference in the localization precision, with THGEM exhibiting a comparatively inferior performance in this regard [26]. With their improved resilience and ease of production, THGEM detectors are especially suitable for experiments that do not require very precise localization resolution [26] and intend to cover a large region.

Working principle of GEMs

The insulation layer between the metal plates on the GEM enables the application of different potentials to each plate. This difference in the applied potential of the metallic electrodes creates a field between the plates which is concentrated in the holes of the GEM,due to the geometry of the structure, as shown in Figure 1.6. Electrons released in the drift region drift towards the holes due to the electric field. As they pass through the hole, they acquire sufficient energy to cause ionization with the molecules of gas filling the structure. The charge amplification occurs within the holes, and most of the electrons generated in the avalanches transfer into the region below the GEM's holes [15]. The electrons leaving the multiplication region can be collected by an electrode or injected on to another GEM to further amplify the signal. The literature reports successful configurations involving the use of GEMs for signal amplification, with evidence demonstrating effective functionality for setups comprising up to five layers [27].

Each hole of the GEM operates independently as a self-contained proportional counter—a distinctive design feature made possible by the shielding mechanism that isolates each hole from its neighboring counterparts [28]. This intentional insulation serves to safeguard the integrity of the counting and amplification processes taking place within each GEM aperture. Furthermore, due to the high number of holes per unit area on the GEM, the gain is not affected by space charge up to very high radiation fluxes [15].

The spatial distribution of charged or ionized particles produced by incident particles interacting with a medium is referred to as an ionization pattern. In the context of GEMs and particle detectors, the ionization pattern is the arrangement or pattern of ionization tracks left by the charged particles as they pass through the gas-filled chamber. The very high spatial resolution that GEMs offer comes in handy in this regard at this means they can precisely record the positions of clusters of primary ionization events created by charged particles. GEM detectors are designed with a uniform electric field and precise geometry, which helps maintain the integrity of the ionization pattern. By preserving the ionization pattern, GEM detectors can accurately reproduce the paths taken by the incident particles as they traverse the gas chamber. This high spatial resolution is crucial in applications where tracking and characterizing the trajectories of particles are essential. The amplification does not significantly alter the spatial distribution of the ionization, meaning the original ionization pattern remains intact but with a greatly enhanced signal.

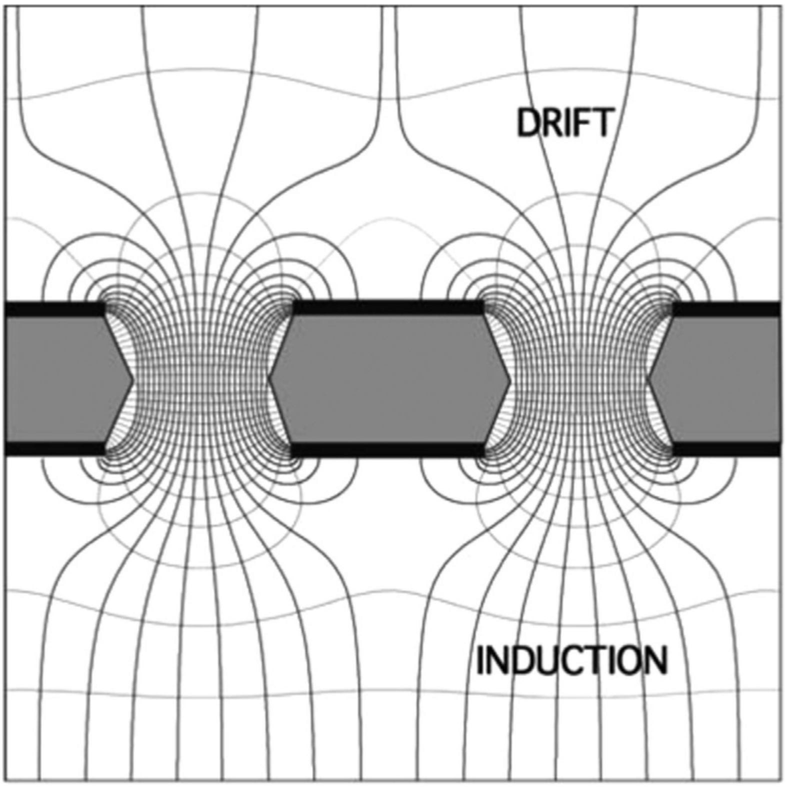

Figure 1.6: Electric field in the region of the holes of a GEM electrode. Taken from [21]

Figure 1.7 shows schematics of a single GEM detector with a two-dimensional readout, the anode. The collection of electrons generates the signal on the anode. The slow-moving ions are gathered on the surface of the GEM. Nevertheless, due to capacitive coupling across the induction gap between the pad plane and the THGEM, there is a small contribution of ions to the signal, known as ion tail [29].

Furthermore, the detector design incorporates a low field between the multiplying and sensing electrodes. This deliberate reduction in the field strength between these two key components serves a critical purpose in the measurements. The low field gap decreases the likelihood of a discharge event propagating toward the sensitive readout electronics. Discharge events, which can involve the sudden release of electrical energy or the movement of charged particles, pose a potential risk to the integrity of the detector and its associated electronics. They can result in both immediate damage and long-term degrada-

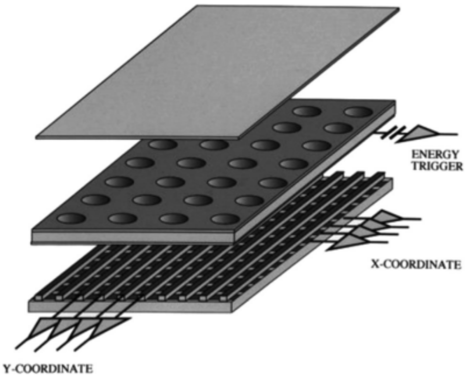

Figure 1.7: Schematics of single GEM detector with two-dimensional readout. Taken from [21]

tion of the equipment.

Yet another essential component of the GEM-based detectors is the gas employed. It is pivotal to consider the gas properties because the choice of gas within the detector plays a crucial role in optimizing its operational efficiency. The gas used in the detector usually consists of counting and quenching gasses. Counting gasses predominates the composition of this mixture. Counting gasses are chosen such that they have a high ionization probability to create and amplify electrons. Noble gases, such as Argon, fulfill this condition due to their electron configuration.

Nevertheless, it is not desirable to use noble gases only because the deexcitation of atoms, which are excited due to the interactions, can cause further signal generation. One method for quenching these discharges is adding a small amount of organic gas, such as methane, to the chamber, which is called quenching gasses [30]. The addition of the quenching gases introduces more degrees into the system and allows the photon, emitted through deexcitation, energy to be converted into vibration. The specific composition of the gas contributes to the detector's ability to accurately capture and amplify signals while mitigating potential risks associated with discharge events and false signals.

1.3 Photocathodes

A photocathode is a specialized surface engineered to utilize the principles of the photoelectric effect. This fundamental process enables the efficient conversion of incident photons, which carry electromagnetic energy in the form of light, into emitted electrons. The unique properties and materials used in photocathodes make them integral components in a wide range of applications, including but not limited to detectors, sensors, imaging devices, and photodetectors. The design, composition, and performance characteristics of photocathodes are of particular interest in detector physics as they directly influence the efficiency, sensitivity, and performance of light-based measurements and detection systems.

Photocathodes often consist of alkali metals with very low work functions or semiconductors with negative electron affinities, such as GaAs, GaInAs, and GaInAsP [31]. CsI stands out for its superior quantum efficiency and responsiveness to vacuum-UV and ultraviolet light [32]. Bialkali materials, such as SbKCs, are used in PMTs, exhibiting a broad spectral response. Furthermore, specialized versions, such as multialkali and extended red multialkali photocathodes, enhance sensitivity in the visible and near-infrared domains, widening the scope of photodetector capabilities [33, 34].

Photocathodes exhibit a range of distinctive properties that are pivotal to their function in converting incident photons into emitted electrons. These properties include spectral response, quantum efficiency, electron yield, and temporal response. Spectral response refers to the photocathode's sensitivity to different wavelengths of light, enabling the selective detection of specific ranges of the electromagnetic spectrum. Not every incident photon on a photoemissive material causes electron emission. The ratio of the number of emitted electrons to the number of incident photons is defined as the quantum efficiency (QE) [35]. QE quantifies the effectiveness with which photons are converted into electrons, a key factor in maximizing the sensitivity of

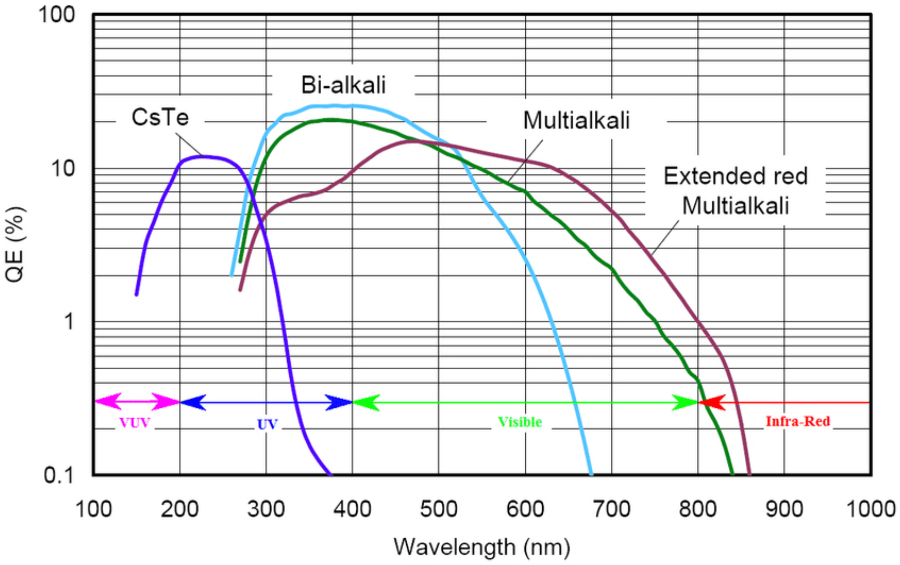

Figure 1.8: Spectral response curves for various typical photocathode materials. Taken from [31].

photodetectors. Figure 1.8 shows the QE of some photocathode materials.

Electron yield measures the total number of emitted electrons per incident photon with the consideration of the QE of the photocathode, influencing the overall signal strength. Additionally, the temporal response characterizes the speed at which the photocathode can generate electrons in response to light stimuli, which is crucial for applications requiring high-speed or time-resolved measurements. An in-depth understanding of these properties is essential for tailoring and optimizing photocathodes to specific experimental requirements and applications.

1.3.1 Photoemission

The electronic properties of ordered, crystalline solids are determined by the electronic band structure of the solid in question [36]. For UV and X-ray excitation, the phenomenological three-step model can be used to explain the photoemission mechanism [37]. Absorbed photons impart some of their energy to the electrons in the material. Then, energized electrons diffuse through the material. Electrons lose some of their energy to collision as they move through the material. Lastly, electrons reaching the surface with sufficient excess energy can escape from the material. Figure 1.9 shows a descriptive sketch of the three phases of the three-step model.

Photoemission

When light is incident on a semi-transparent surface, which is the characteristic of the photocathodes used in this thesis, only a fraction of photons impart their energy to the electrons in the material. The photons that do not impart their energy are either reflected

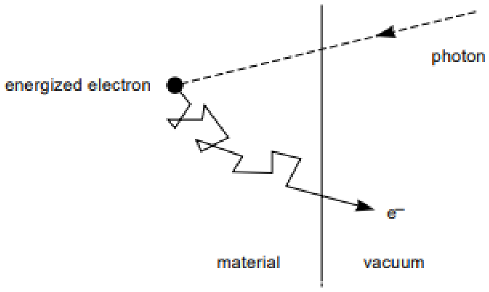

Figure 1.9: Photoemission described by three-step model. Taken from [35]

from the front or back of the layer or pass through it and, therefore, do not contribute to the photoemission. Flux absorption as a function of the distance from the surface is given by the general equation

$$\frac{d\phi_p(\nu,x)}{dx} = -\alpha(\nu)\Gamma(x)\phi_p(\nu,x) \tag{1.6}$$

where $\alpha(\nu)$ is the absorption coefficient of the material, and the complex function $\Gamma(x)$ takes the reflections from both surfaces into consideration[35]. The absorption coefficient depends on the energy of the photons and the properties of the material.

In a slice with thickness dx, the number of electrons, n, excited by the transfer of photon energy is proportional to the flux absorption.

$$\frac{dn}{dx} = -\alpha_e \frac{d\phi_p(\nu,x)}{dx} \tag{1.7}$$

where the proportionality is represented by the α_e term [35].

Electron diffusion

The energy-loss mechanism controlling an excited electron's journey to the photocathode's surface determines the likelihood that it will be released. Depending on the properties of the photocathode, this process is different. For example, the procedure for a photocathode that is a semiconductor differs from the metal one.

The conduction band of semiconductors is nearly empty, and the probability that excited electrons will collide with other free electrons while diffusing through the conduction band is very low. Therefore, the energy loss is mainly due to the creation of phonons and is very low [35]. Thus, excited electrons can travel relatively long distances through the material before reaching thermal equilibrium. Due to the existence of an energy barrier at the surface of the semiconductor, electrons in thermal equilibrium are impossible to emit; only the ones that have retained an excess of energy can escape into the vacuum.

Surface barrier

The Fermi level, E_f, is in the forbidden band in semiconductors. The valence band- with the upper limit E_v- is almost completely full, whereas the conduction band- with a lower limit E_c- is almost empty. Therefore, for photoemission to occur, the electrons in the valence band should gain sufficient energy to overcome the band-gap energy, E_g, and the electron affinity, E_A, of the conduction band [35]. Thus, the photoemission threshold of a semiconductor, W, is given as follows:

$$W = E_g + E_A \tag{1.8}$$

This threshold is also called the work function of the surface.

Given the specific conditions influencing photon absorption and the inherent energy losses experienced at each stage of the photoemission process, it is important to note that the QE is always less than one. Several factors contributing to this phenomenon are the wavelength of the incident light and the composition and thickness of the photoemissive material.

1.4 THGEMs for Photodetection

In the pursuit of advancing the capabilities of photodetection systems, the synergistic integration of photocathodes and GEMs emerges as a promising avenue for achieving heightened sensitivity and precision. This approach capitalizes on the distinct advantages of photocathodes in efficiently converting incident photons into electrons and the amplification capabilities of GEMs in boosting the ensuing electron signal. Furthermore, the utilization of a THGEM instead of a GEM also allows the production of more stable and resilient detectors. The amalgamation of these components holds significant potential, particularly in applications that demand a huge detection area. However, realizing this potential requires a meticulous exploration of the feasibility, challenges, and opportunities inherent to the combination of photocathodes and THGEMs for photodetection. Studies have investigated the application and the properties of coated THGEMs in photodetection scenarios [38, 39]. Building on the knowledge obtained from investigations into the properties and applications of THGEMs in photodetection, THGEMs are actively employed in detectors such as COMPAS RICH-1 and HADES RICH [40, 41, 42].

The basic working principle of a THGEM-based photodetector is shown in Figure 1.10. A photon enters the detector and passes through a mesh. Although the mesh is not a necessity for the system, it acts as a barrier for unwanted particles which could cause noise in the detector. Then, the photon interacts with the photosensitive layer, ejecting an electron from the surface. For this reason, the choice of the photocathode material plays a crucial role so that the photons of the measurement can impart enough energy to overcome the work function of the surface. The primary electrons drift in a moderate electric field towards the GEM and are sucked into the GEM holes, where the field is higher as a result of the geometry of the THGEM. Within the holes, the high field leads to the avalanche multiplication. The amplified electrons exit the GEM hole. Depending on the number of primary electrons ejected, further multiplication might be needed, in which case multiple layers of THGEMs could be used as described previously. Lastly, after sufficient amplification of the initial signal, an electric

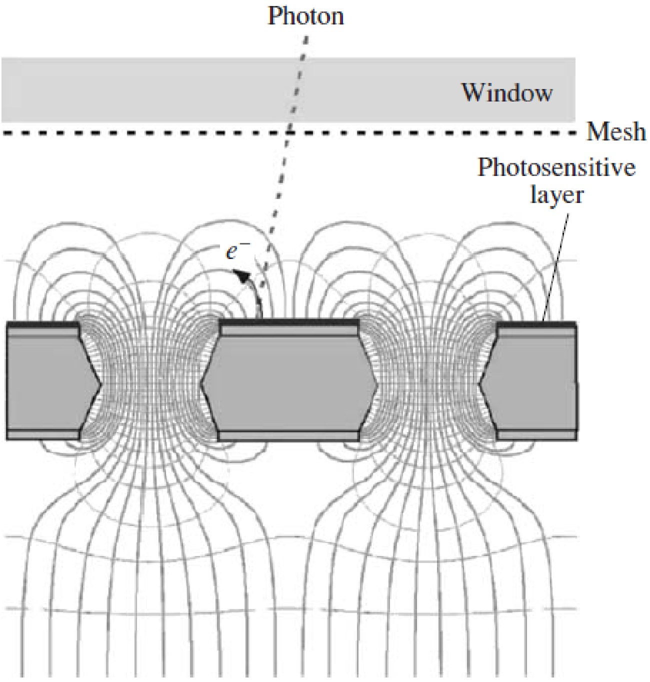

Figure 1.10: Working principle of photodetector with photocathode coated GEM. Taken from [43]

field moves the electrons to the anode. The systems employing GEMs and THGEMs share virtually identical configurations, see Figure 1.7, with the sole differentiator being the type of gas electron multiplier utilized.

2 Experiment

2.1 The Detector

In this investigation, all the measurements take place in an aluminium vessel. The vessel has a volume of around 7 liters. The vessel and components fixed to it are shown in Figure 2.1. It is consists of two pieces; a body and a lid. An O-Ring is placed between the lid and the main body to ensure better seal for the vacuum. Furthermore, the lid and the body feature matching holes, through which threaded rods are inserted. These threaded rods, which can be seen in the Figure 2.1, serve a dual purpose: they secure the lid to the body, and they ensure alignment between the two components.

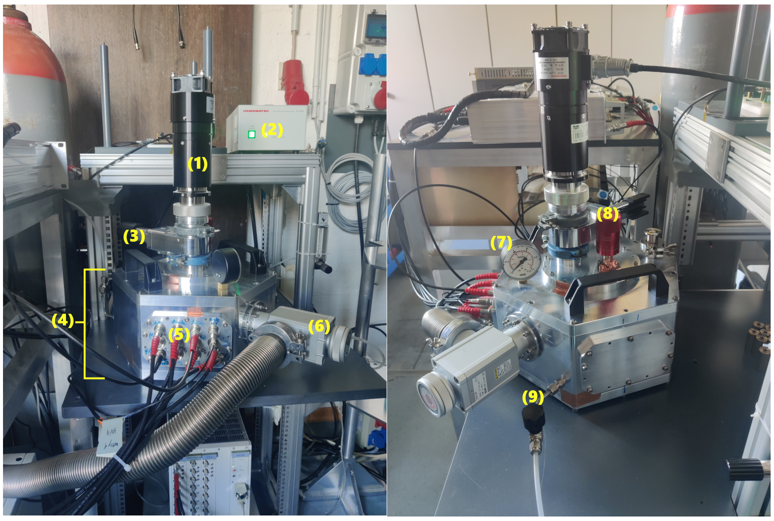

(1) UV Lamp

(2) Power supply for lamp

(3) Lever

(4) Vessel body and lid

(5) SHV feedthroughs for pA meter connection

(6) Valve for the vacuum pump

(7) Manometer

(8) Filter wheel adjustment knob

(9) Gas inlet for flushing

Figure 2.1: The detector vessel and parts fixed on it.

The experimental setup comprises a lamp integrated into the vessel lid, with a connection mechanism featuring a lever that can be used to block the light. As a light source a Hamamatsu H2D2 unit L15094 is used. Figure 2.2 illustrates the spectral distribution, directivity -light distribution-, and light irradiation range of the deuterium lamp. The wavelength spectrum of the used deuterium lamp has a peak for wavelengths around 161 nm due to the built-in MgF_2 window [44].

The vessel also has a manometer fixed onto it which is used to gauge the pressure inside the vessel. Moreover, 8 SHV feedthroughs are connected to the vessel wall which allows the connection of electrodes to the measurement devices.

Quantum efficiency of a photocathode is defined at certain wavelenghts of light. Because of that it is benefical to add a filter to the opening of the monochromatic light source. In this setup there is a filter wheel located underneath the detector vessel lid for the filtration of certain wavelengths,the filter wheel is shown on Figure 2.3. The filtration wheel has holes wherein the different optical windows can be placed. The position of wheel can be adjusted

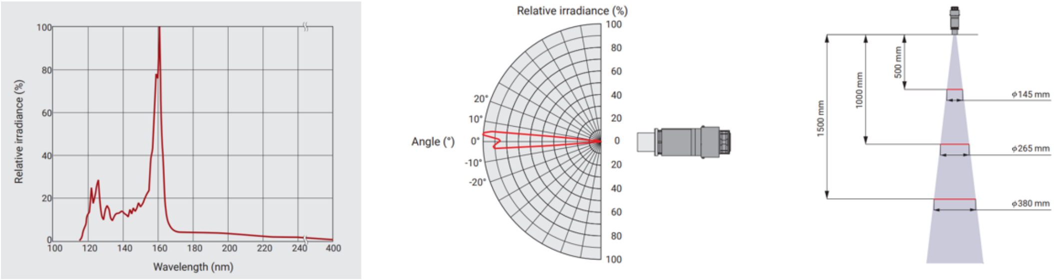

Figure 2.2: Technical information of the lamp: Wavelength distribution (left), directivity (middle), and light irradiation range(right). Taken from [44]

using the knob fixed to the lid, this allows the filter to be changed without opening the lid. The filters present on the wheel and their position in degrees are shown on Table 2.1.

Filter	192 nm	171 nm	SiO_2	CaF_2	None, smal	None, big	Closed
Position [degrees]	82	124.5	170	220	226	313	356

Table 2.1: Types of filters on the wheel and their position

In the context of the experimental configuration, the vessel described earlier is an integral component. Its interaction with the overall setup is crucial as it houses the THGEMs, when used, photocathode and the readout system. The detector vessel forms an essential element in overall experimental framework. Figure 2.4 provides a comprehensive overview of the operational setup employed in the experimental configuration. The gas bottle in the figure contains a mixture of Ar and CH_4 in a 90-10 ratio. In this mixture, Ar is used as the counting gas, whereas CH_4 is the quenching gas. Additionally, the figure highlights essential instruments: the Keithley electrometer, the pA-meter, the vacuum pump for maintaining controlled conditions, and the high voltage supply. Finally, the FPGA board is a pivotal element responsible for controlling and processing data within the experimental framework. As a whole, these components, thoughtfully illustrated in Figure 2.4, collectively constitute the operational core of our research setup, facilitating precise and controlled experiments essential to the investigation.

The vessel detector houses a modular rig which allows the different setups to be used for measurements. In the scope of this thesis two primary modes of measurement are used: Reflective mode and transmissive mode. Transmissive quantum efficiency measurement assesses how efficiently a material or device converts incident light that passes through it into an electrical current. It's particularly relevant for photodetectors and solar cells. On the other hand, reflective quantum efficiency measurement evaluates the same property in a different configuration. These measurements provide insights into the effectiveness of materials and devices for their intended applications.

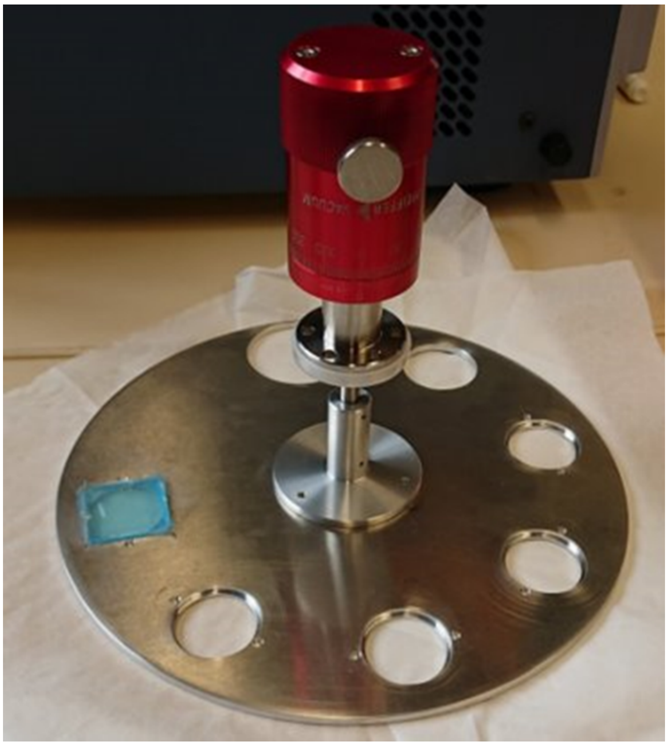

Figure 2.3: Filter wheel removed from the detector vessel lid

2.1.1 Reflective Mode

In the reflective mode, the readout is located on top of the measured sample. The setup sketch can be seen in the left side of the Figure 2.5. From top to bottom, the setup consists of an aperture, a wire mesh, a wire plane, the sample, and the sample holder. The specific design of the sample holder varies based on the sample in use, a detail to be elaborated shortly. The aperture is placed at the top, serving to maintain the illumination area constant while allowing us to gauge the performance of the incident light.

Beneath the aperture, a wire mesh is strategically positioned. Its primary function is to act as a filter, effectively preventing ions and electrons from traveling downward and interfering with the measurements. This is crucial for ensuring the accuracy of our data.

Directly below the wire mesh, a wire plane is located, to which the pA-meter is connected. The purpose of this wire plane is to facilitate the measurement of electrons ejected from the sample during the experiment.

2.1.2 Transmissive Mode

Measurements in transmissive mode employ amplification, as the primary electrons cannot create a measurable signal by themselves. Therefore the detector is filled with gas during transmissive mode measurements. In this thesis, the choice of gas for our gaseous particle detector system is Ar-CH_4 (90-10) , where methane serves as the quenching gas. The same

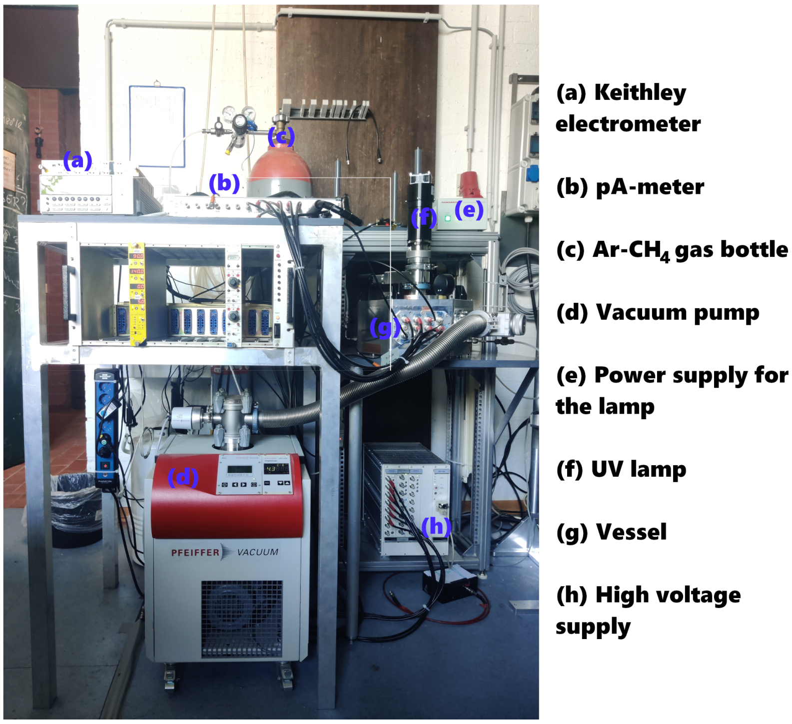

Figure 2.4: General setup used in the experiment

gas mixture, with a different ratio, is also used in COMPAS RICH because it ensures effective extraction of photoelectrons from the photocathode [45] The selection of this specific gas mixture is pivotal in determining the performance and safety of the detector. CH_4, in its role as a quenching gas, plays a multifaceted role in the operation of the detector. Its primary purpose is to ensure the safety and stability of the detector by promptly stopping any ongoing discharge or electrical breakdown. Additionally, CH_4 contributes to controlling the recovery time of the detector, preventing saturation, and maintaining the efficiency of particle interactions. This controlled and deliberate choice of quenching gas is instrumental in achieving the precise and reliable results necessary for our experimental objectives.

In the transmissive mode, the arrangement of layers differs significantly, as seen in the right side of Figure 2.5. The sequence from top to bottom is designed to serve distinct purposes.

Starting at the top, we have the sample holder, which plays a vital role in securing the sample in place. Additionally, it applies the necessary pressure to ensure a reliable connection with the sample. This connection is crucial for photocathode to work properly.

Directly below the sample holder, two GEMs, THGEM 1 and THGEM 2, are positioned. These GEMs serve to amplify the primary electrons ejected by the sample. Their amplification function is of paramount importance as it enables detection and measurement of faint signals that would otherwise be unmeasurable. Lastly, at the bottom of the layer sequence, we find the pixel pad, which acts as the readout. The pixel pad not only allows us to measure the strength of the signal but also pinpoints its location precisely.

The unique configuration of layers in the transmissive mode optimizes the experimental

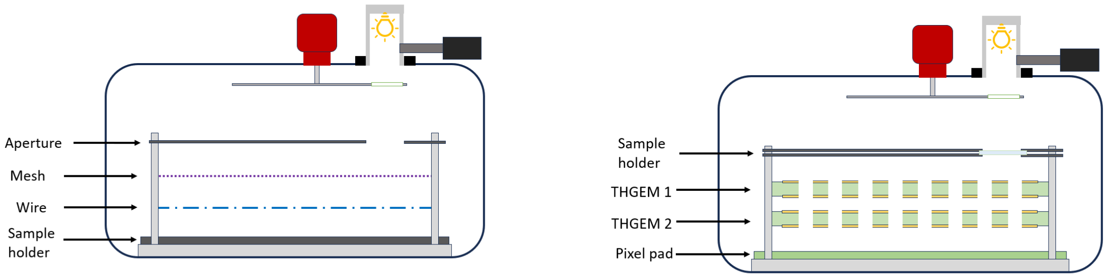

Figure 2.5: Paths taken by electrons and ions released from the hole of the aperture (left) and above the mesh plane (right).

setup for measuring and analyzing the sample's characteristics, ensuring both the reliability and precision of the data collected.

During initial setup tests, it was observed that frequent discharges were occurring within the detector. Within this configuration, there exists a potential risk of discharges occurring between these layers, posing a threat to the integrity of the detector. To mitigate this risk, we have implemented a protective measure by connecting $10\,\mathrm{M\Omega}$ resistors to the both sides of the THGEMs. While this addition does not diminish the likelihood of a discharge, it effectively prevents continuous discharges by extending the time required for the electrodes to recharge.

2.1.3 The Readout System

In our experimental setup, we employ different readout anodes for transmissive and reflective modes to meet specific measurement requirements. The wire plane is used for reflective mode, while the pad plane is dedicated to transmissive mode. These anodes are integral components for detecting and recording particle interactions with the detector. The following sections provide detailed insights into the wire plane and pad plane, highlighting their distinct functions and roles in our research.

Wire plane

The wire plane, a fundamental component of our reflective measurement configuration, consists of a square PCB frame, see Figure 2.6 . Spanning across this frame are a network of fine wires, meticulously arranged to cover the empty region. These wires are intricately connected to gold strips on the PCB, creating a conductive pathway. The gold strips then link the wire plane to the pA-meter through a $10\,\mathrm{M\Omega}$ resistor. This carefully designed setup serves the crucial function of detecting electrons ejected from the sample positioned below the wire plane.

The selection of the wire plane as the anode for reflective measurements is guided by the unique demands of this mode. In reflective measurements, the incident light originates from above, necessitating the use of a transparent or transmissive anode that allows the incoming

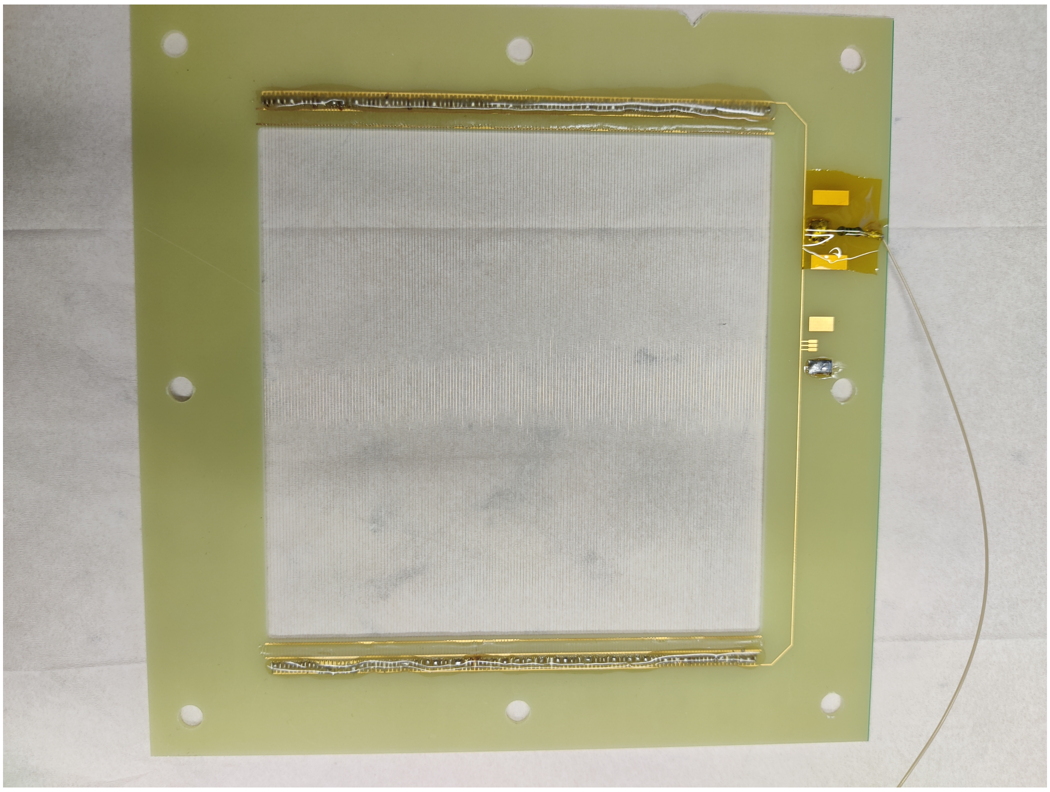

Figure 2.6: Wire plane consisting of wires placed across a Kapton frame

photons to penetrate. Simultaneously, this anode must possess the capability to efficiently detect and record electrons emitted from the sample situated below. The wire plane, with its transparent design and adeptness at capturing and transmitting the electron signals, aptly fulfills these specific requirements. Its sensitivity and structural compatibility make it the ideal choice for our reflective measurement setup. Nevertheless, it should be noted that this choice also has its shortcomings for example with this configuration there is no space resolution for the signal.

Pad plane

In the transmissive setup of the experiment, a multi-pad anode is employed due to its structural advantages. This configuration enables the measurement of signals at various positions by reading out individual pads. The use of a multi-pad anode provides the flexibility to capture and analyze signals from different locations, contributing to a more comprehensive understanding of the experimental outcomes

In order to have spatial resolution and improve performance of the detector a new anode, designed by Leonardo Bugia [46], is utilized instead of the wire plane. The new multi-pad anode is then assembled with new connectors providing the flexibility to modify connections from outside the detector vessel. Figure 2.7 show the new multi-pad anode.

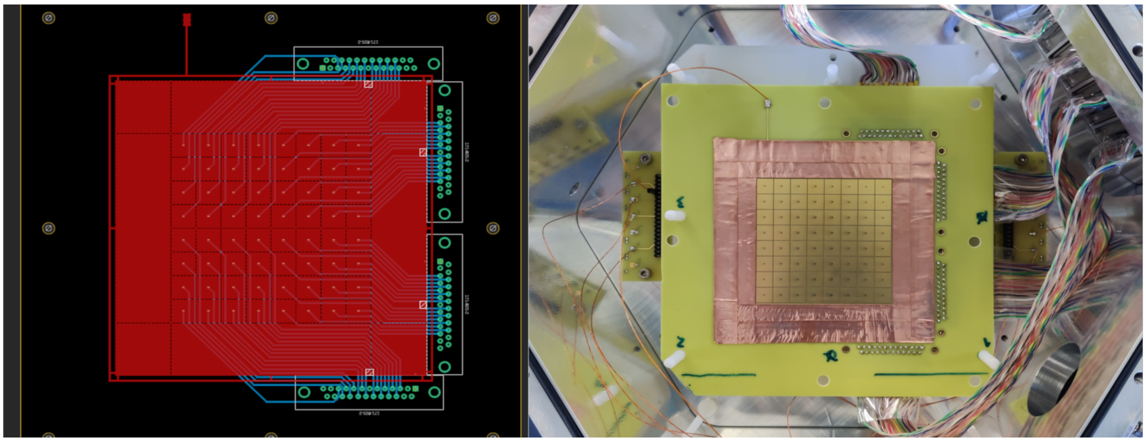

Figure 2.7: A picture of the new Multi-Pad-Anode design on Autodesk Fusion360 (left) and the anode installed in the detector vessel (right)

As mentioned previously, the new anode design aims to enable us to change the cables within detector without compromising the vacuum or the inert gas environment within the detector. For this reason the side panel of the vessel is modified. Four Sub-D-25 connectors are connected to the bottom of the anode to read each pad individually. These connectors are then connected to gas-tight Sub-D-25 feed-through connectors, embedded into the side panel modified for this purpose. The modified side panel and the mapping of the pad plane is presented in Figure 2.8. This configuration allows the measurement of the individual pads without opening the chamber.

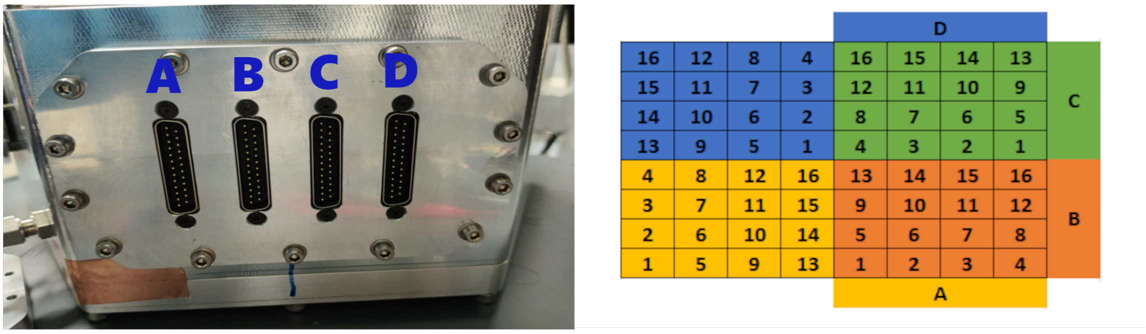

				D				
16	12	8	4	16	15	14	13	C
15	11	7	3	12	11	10	9	
14	10	6	2	8	7	6	5	
13	9	5	1	4	3	2	1	
4	8	12	16	13	14	15	16	B
3	7	11	15	9	10	11	12	
2	6	10	14	5	6	7	8	
1	5	9	13	1	2	3	4	
				A				

Figure 2.8: Modified side panel of the detector vessel (left) and the mapping of the anode(right)

Figure 2.9: Interior of the coating chamber with an inserted THGEM (left), and a picture taken during the coating procedure where the blue glowing circle is the CsI pill(right). The right side picture is taken from [47]

2.2 Sample Preperation

2.2.1 CsI Coated Sample

The THGEMs are coated with cesium iodide at a clean room facility in the physics department at the TUM. The THGEMs used during this bachelor's thesis have a total area of $18 \times 18\,\text{cm}^2$. They are made out of 500 µm layer of FR4, a base material made from epoxy resin and glass fabric composite, copper layers coated with 5 µm thick gold layer. The active area of the THGEM is $11.3 \times 11.3\,\text{cm}^2$ and is divided into 37.5 cm sections, with a hole to surface ratio of 0.2267.

The deposition of CsI layers is performed in a high-vacuum environment by electron beam evaporation from a pressed tablet of CsI powder, called a CsI pill. Therefore, the coating procedure takes place in a vacuum chamber. The THGEM that will be coated is put in a chamber upside down. The air inside the chamber is pumped out. The CsI pill, which is located underneath the THGEM, is heated and evaporated onto the surface via electron beam operation. A picture of the coating chamber with the CsI pill is shown in Figure 2.9. An aperture is located between the THGEM and the CSI pill this limits the coating are to be two rectengles located on different sections with an area of 2 x 4 cm. The coated region on the THGEM can be seen on Figure 2.10. The details of the coating procedure at the TUM facility are explained in detail in papers regarding the coating of the HADES RICH mirrors [48]. It should also be noted that, in the scope of this thesis, heat treatment, which improves the quality of the photocathodes [43], is not performed.

2.2.2 Diamond-like Carbon (DLC) Coated Sample

Thin carbon films can be produced using different methods such as evaporation-condensation, laser plasma ablation-deposition, and glow discharge in ethene gas [49]. The samples, made at

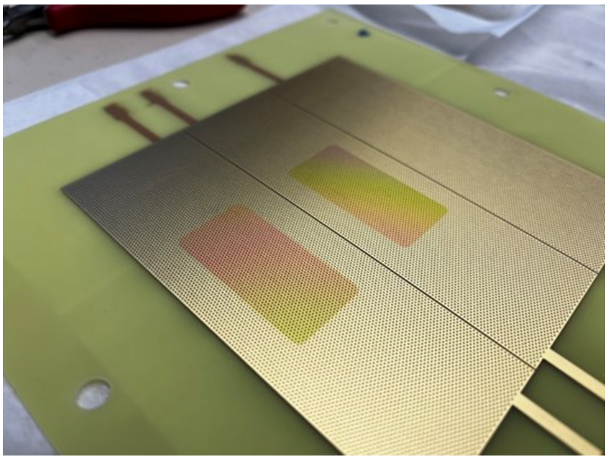

Figure 2.10: CsI coating on the THGEM

TUM, are produced with laser plasma ablation-deposition.

Firstly, a carrier is prepared by applying a betaine solution to a glass plate. The solution dries, resulting in small betaine crystals growing on the substrate. Then, the betaine layer is covered with $100\,\mu g\,cm^{-2}$ of copper. This extra layer makes it possible for the deposited carbon film to be released from the substrate, which is known to be an issue for films deposited with high laser beam intensities [50].

The carrier is then placed inside a vacuum chamber with a graphite target. Once the air within the chamber is pumped out and a high vacuum is established, the graphite target is radiated by a pulsed nd:YAG laser. A hot plasma is induced by irradiating the target material, which ablates the graphite.

Following the deposition of single atoms onto the carrier, a combination of sp2 and sp3 hybridized carbon emerges. Within the DLC, a substantial fraction of sp3 type C bonds are present [51].

Once the DLC layer is formed, it needs to be removed from the carrier materials to be transferred onto experimental samples. The glass plate is immersed in distilled water, which causes the betaine layer to dissolve. This process releases the layer of copper with DLC from the glass plate. Then, the copper layer is dissolved in nitric acid, leaving the DLC layer behind. Figure 2.11 illustrates the successive steps involved in the isolation of the DLC layer. Lastly, this layer of DLC can be transferred onto the carrier- a frame or a metal plate- to be used in the experiment.

Within the experimental framework, our self-prepared samples, detailed in the preceding section, are complemented by MgF_2 windows coated with DLC. These windows are produced by CERN.

2.2.3 Sample Holder

We employ varying sample holder designs, tailoring each to the specific requirements of the sample under investigation. The sample holder must meet specific essential criteria regardless

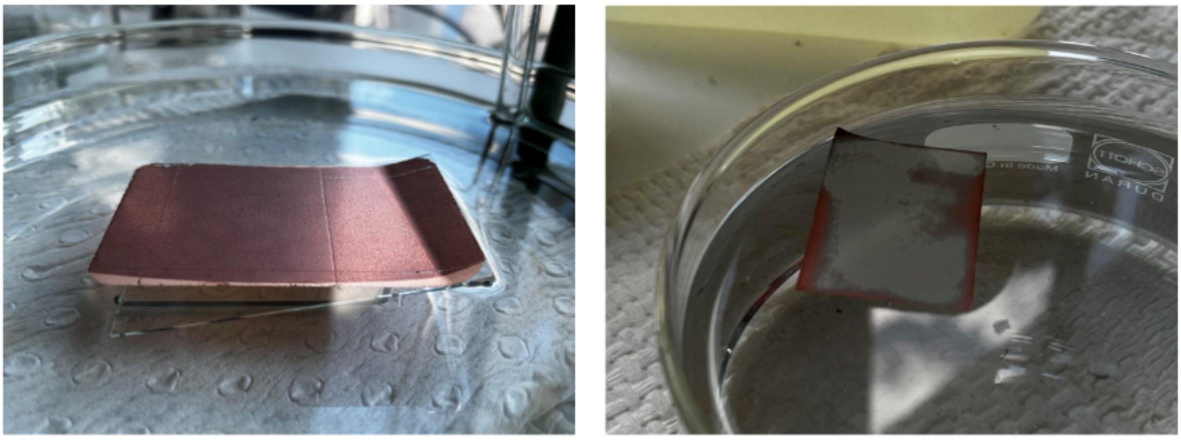

Figure 2.11: Glass plate in water (left) and carbon layer on copper in nitric acid (right). Taken from [52]

of the sample type. Firstly, it must ensure the stable and consistent positioning of the sample during every measurement, eliminating variations in the sample's location that could introduce inaccuracies.

Additionally, the sample holder plays a pivotal role in facilitating the connection between the sample, the power source, and the pA-meter. This connection is crucial for enabling the photocathode to function as intended. The absence of a reliable connection compromises the entire measurement process, a fact validated through preliminary testing. Therefore, the sample holder's design and performance are fundamental to the experiments' success and accuracy.

Figure 2.12: Different sample holder types: sample holder for metal plates (left), sample holder for the frames (middle), sample holder for glass window (right)

Within this thesis, three different sample holder types, shown in Figure 2.12, were used. For the first type, a plastic plane with a groove holds the plate in a fixed position for DLC coated metal plate, and a hole on the plane secures the metal plate onto the sample holder. The screw also holds the cable that connects the metal plate to the pA-meter.

The second type addresses DLC stretched across frames with varying thicknesses. An 18 ×

18 cm^2 plastic plane is used, featuring holes beneath the lamp opening that serve as fixtures for diodes. This configuration allows for the determination of DLC thickness-dependent light transmissivity.

The third type is tailored for insulating materials like DLC or CsI-coated MgF_2. It consists of two sand-brushed aluminum plates with grooves to hold the glass window. These plates are securely fastened together with screws and spacers. The spaces ensure that a constant pressure is applied to the sample. A cable is fixed to the aluminum plate to connect the photocathode with the power source and the pA-meter. This design accommodates the unique challenges posed by insulating materials, allowing for precise measurements and accurate data acquisition.

2.3 Simulation

In this study, we delved into the properties of the reflective mode by using a 3D model and various simulation software; COMSOL Multiphysics and Garfield++. Our pursuit of understanding is driven by the challenge of balancing accuracy with computational feasibility. Consequently, our model introduces simplifications, such as rescaled wire planes and substituted wire meshes, addressing the complexities that could otherwise overwhelm simulation programs. As we undertake this investigation, our objective is to reveal the intricacies of the reflective mode's behavior across diverse voltage conditions. Our focus involves a detailed analysis of the electric fields within the setup, closely examining how the system responds to subtle adjustments in key parameters.

2.3.1 Building the Model

The individual layers of the detector are made using Autodesk Fusion360. For the most part, the model is a one-to-one replica of the setup. Nevertheless, simplifications to the model geometry were made to overcome computational constraints. Figure 2.13 shows a rendering of the model created on Fusion 360 without the mesh itself.

The aforementioned simplifications are made on two different layers of the detector: the wire plane and the wire mesh. Firstly, the size of the components of the wire plane is increased while keeping the ratio of the dimensions between the pieces constant. For example, the wire pitch is increased to 1.25 mm from 1 mm. Notably, the intricate 18 µm stainless steel wire mesh, a crucial element of the actual setup, posed a computational challenge. The mesh plane used in the experiment consists of an interwoven wire mesh, with a wire thickness of 18 µm and wire pitch 45 µm, sandwiched between two Kapton frames. Due to its intricacy, any attempt to create a one-to-one copy of the wire mesh exceeded the capabilities of both the design software and the simulation program. Therefore, the wire mesh is substituted with a more computationally friendly square plate with periodic square holes.

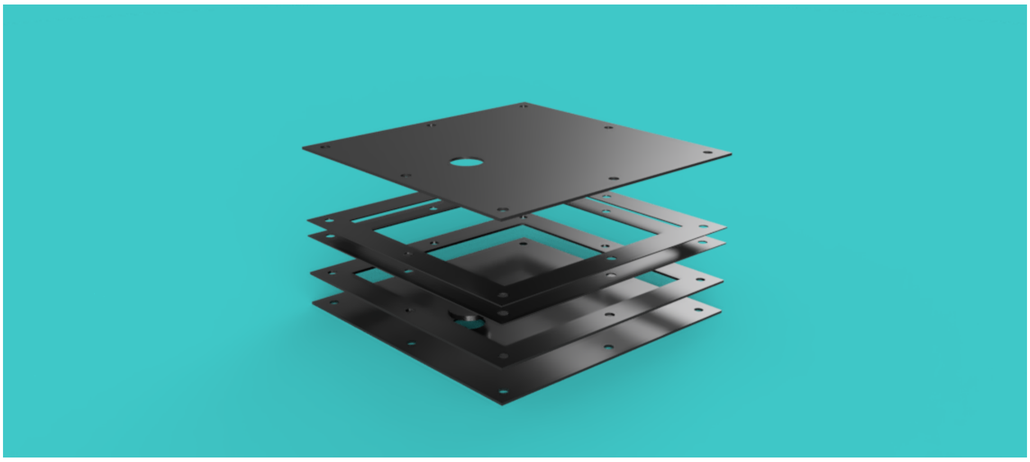

Figure 2.13: A rendering of the model where the layers are put in their proper order

2.3.2 Simulating in COMSOL

COMSOL Multiphysics is a finite element analysis, solver, and simulation software package for various physics and engineering applications. COMSOL can create physics-based models, and various physical parameters can be simulated using this model. After creating the 3D model in Autodesk Fusion 360, it was imported into COMSOL Multiphysics to analyze the electric fields within the setup under varying voltage conditions.

Once the model is constructed in COMSOL, the components of the model are assigned their respective materials, giving them their physical properties. All electrodes were assigned as copper, the insulator layers and frames with Kapton, and the rest of the volume as argon gas. This assignment of material also allows the relative permittivities of the material to be imputed into the model which is crucial information for Garfield++. The relative permittivities are set to 1, 4, 1e10 for argon, Kapton, and copper respectively. The next step is to define the electric potentials of the electrodes with the use of the electrostatics module included in the COMSOL. This module allows the user to select surfaces of the model and assign electric potentials to them.

After the properties of the detector and the associated fields are all defined, one can start the calculation of the fields. It is also possible to perform a parametric sweep by assigning parameters to the predefined values. This allows us to adjust multiple parameters at a time and investigate all the possible combinations with these parameters. Nevertheless, increasing the number of combinations causes the calculation time to rise exponen-

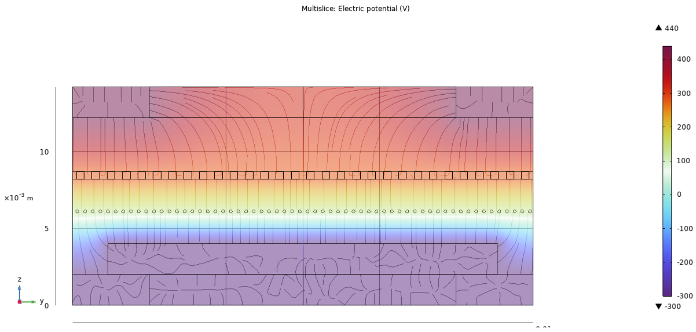

Figure 2.14: Example field configuration on COMSOL

tially. Therefore, the number of parameters during a sweep is kept low.
Then, COMSOL creates an electric field map of the defined geometry. An example of a field map was plotted with field lines in Figure 2.14. COMSOL also creates the necessary files for the Garfield++; the mesh of the detector, and field information.

Firstly, we conducted an assessment of the impact of the aluminum vessel containing the detector on the overall measurement accuracy. Specifically, we investigated whether the walls of the detector introduced interference, potentially influencing the measurements. The simulation results revealed that in the proximity of the measurement region, the edge effect was found to be negligible. Armed with this understanding, we implemented a mirror-symmetric basic volume of the model in the simulation. This adjustment not only substantially alleviated the computational burden but also expedited the simulation runtime, all the while preserving the precision and reliability of the obtained results.

Moreover, it is possible to calculate the electric field at a specific point inside of the detector. Combined with the parameter sweep, this allows us to gauge the strength of the electric field components and their sum depending on the configuration. The results of such sweep showed that, between the wires, the total field strength is dominated by the component horizontally perpendicular to the orientation wires, which is expected as the experimental setup aims to collect electrons at the wires.

The simulation in COMSOL provided valuable insights into the distribution and intensity of electric fields within the reflective mode setup. We systematically adjusted the voltage settings and explored how different parameters influenced electric field patterns and strength. This comprehensive analysis serves as a crucial foundation for understanding the system's behavior in response to varying voltage inputs.

2.3.3 Simulating in Garfield++

Garfield++ is an object-oriented toolkit designed for detailed particle detector simulations, focusing on ionization measurements in gases or semiconductors. Its capabilities include calculating electric fields using solutions in the thin-wire limit, interfaces with finite element programs, and connections to tools like Synopsys Sentaurus and neBEM field solver[53]. Moreover, Garfield++ possesses advanced visualization capabilities, allowing for the creation of compelling visual representations that illustrate the intricate dynamics simulated within the particle detector, see Figure 2.15 for example.

Three essential files are required to execute a simulation in Garfield++: a mesh file, a field file from COMSOL, and a dielectrics file- manually inputted material properties. The dielectrics file specifies the number of materials, their relative dielectric constants, the number of domains, and a list of domain indices with corresponding material indices.

Once the dielectrics file is imported to Garfield++, the mesh file- containing the geometric structure of the detector- and the field file- delineating electric field distributions under various conditions- are also imported into Garfield++. This integration lays the foundation for the continuation of the simulation process, as it capitalizes on the detailed information generated by COMSOL.

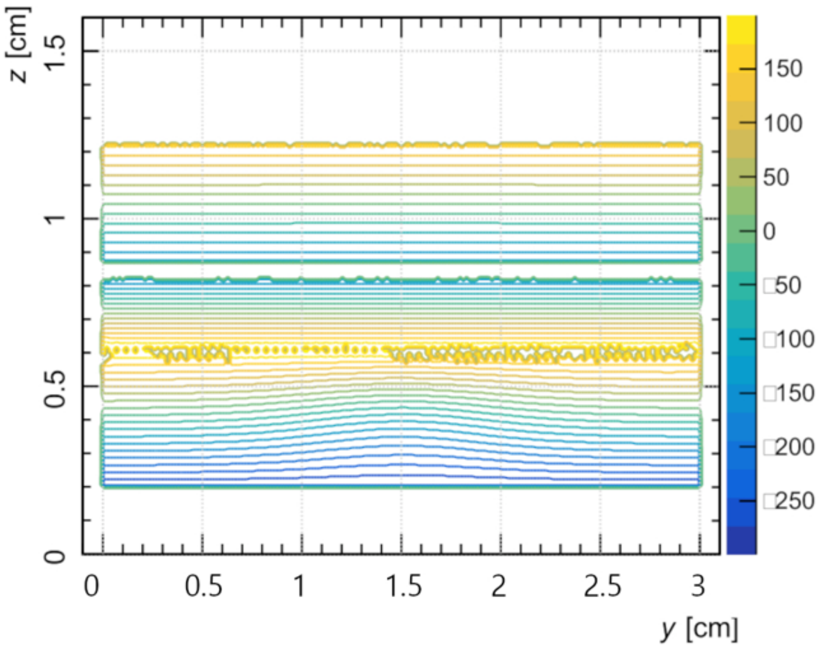

Figure 2.15: Contour of the electric fields within the detectors measurement region in reflective setup

With the requisite files in place, the simulation is initialized within Garfield++. Configurations are set to define parameters such as the properties of the gas within the detector, the starting point of the electrons, ion transport properties, and electron collision rates.

Electron avalanches are simulated using a microscopic Monte Carlo method based on the electron-atom and electron-molecule cross-sections in the database of the Magboltz program [53]. The algorithm inputs the collision rates as a function of the electron's kinetic energy for each scattering mechanism that can take place in the gas. The user can set the maximum energy; for avalanche calculations, the electron energy is chosen between 50 eV to 200 eV.

Within the examination of the behavior of electron-ion pairs, as depicted in Figure 2.16, two graphs outline the trajectories of electrons and ions within the detector. The simulations show a distinct pattern: electrons situated above or within the aperture gravitate towards it for absorption to the aperture. At the same time, ions are purposefully guided towards the mesh, effectively stopping their reach to the readout electronics. This underscores the critical role of the mesh in sculpting the trajectories of particles within the detector setup and ensuring that no unwanted particle reaches the readout electronics.

In our exploration to ensure the detector operates as intended, we deliberately varied field configurations for electrons. This deliberate implementation of various configurations served a dual purpose: firstly, it aimed to confirm the expected behavior established during the detector's design phase. Additionally, during practical measurements, certain configurations

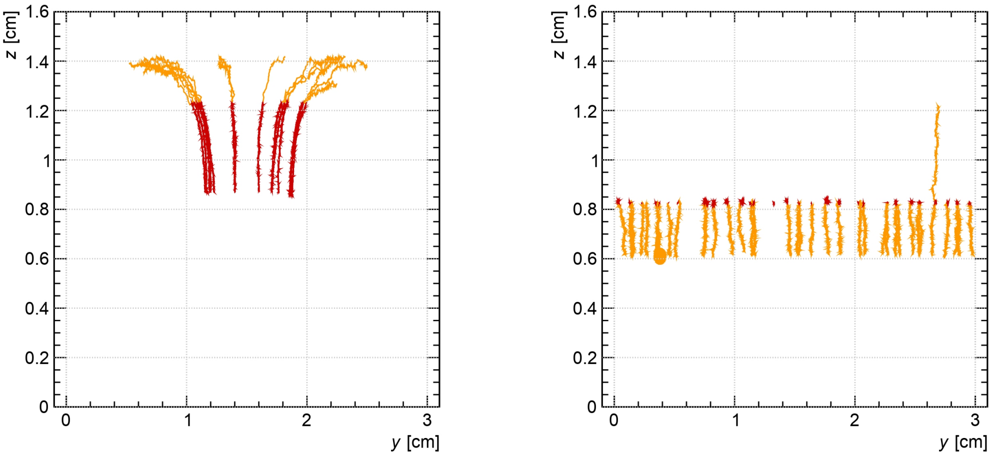

Figure 2.16: Paths taken by electrons and ions released from the hole of the aperture (left) and above the mesh plane (right).

exhibited outliers. Simulations were conducted to determine whether these outliers were rooted in hardware limitations or inherent physical phenomena. Remarkably, the simulations revealed no noticeable differences in the trend for the different configurations, strongly suggesting that any observed variations during measurements were more likely attributed to hardware abnormalities than genuine physical phenomena.

In Figure 2.17, a comprehensive portrayal of electron paths unfolds, providing valuable insights into the behavior of electrons released at various heights within the detector. Notably, electrons released beneath the wire plane at a height of 6 mm exhibit a distinctive pattern: they are uniformly drawn towards the wire plane. This observation suggests minimal to no loss in registering electrons ejected from the sample, affirming the robustness of the measurement process.

The remaining sections of the detector reveal a noticeable trend in electron movement. Electrons positioned above or within the aperture undergo redirection toward the aperture, indicating a deliberate mechanism preventing their entry into the detector volume. Similarly, electrons released between the aperture and the mesh plane follow a path leading them towards the aperture. This alignment with the aperture's influence is crucial, as it suggests that the measurements are unlikely to be influenced by external electrons.

In the vicinity slightly above the mesh, a nuanced behavior is observed. Some electrons are directed upward, while others are guided toward the wire plane. This dual trajectory aligns with expectations, considering the pronounced strength of the electric field in the region between the mesh and the sample. This intricate interplay of electron paths, as illustrated in Figure 2.17, provides a comprehensive visual understanding of the detector's response to electrons released at different heights, further validating the reliability of the measurement setup.

Integrating Garfield++ with COMSOL Multiphysics expands the study's scope, providing

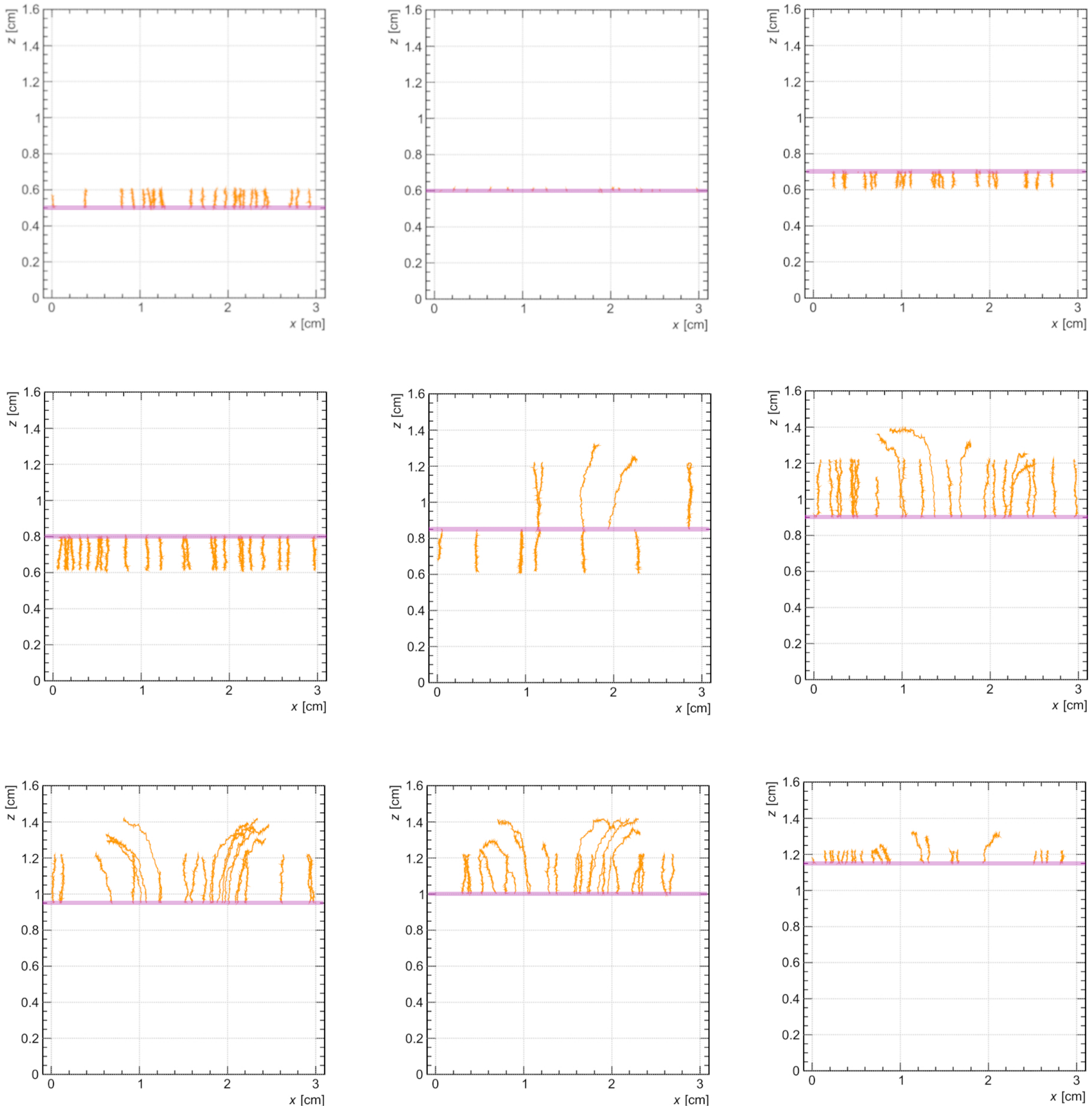

Figure 2.17: Path of the electrons released from different heights within the detector. The purple line shows the height from which the electron is released in the simulation. Note that the purple lines are added in photoshop.

a nuanced understanding of the reflective mode's underlying physics. This combination leverages the unique strengths of each simulation tool, establishing a solid foundation for a holistic investigation into the reflective mode's properties.

2.4 Measurement Procedure

2.4.1 Determination of Quantum Efficiency in Reflective Mode

To calculate the quantum efficiency, QE, we need to determine the ratio of emitted electrons from the photocathode and the number of photons incident on the photocathode.

The number of incident photons can be extracted using a reference measurement with a diode whose QE is known. This measurement is made with a Thorlab FGAP71 diode with an active area of $2.5 \times 2.5\,\text{mm}^2$. The diode is placed on the sample's location, ensuring that the distance to the lamp is the same. Every other electrode is left in its original place; thus, we can assume that the same number of photons will hit the unit area.

The reference measurement begins by starting the vacuum pump and leaving it to pump for several hours to reach a pressure around $p = 5 \times 10^{-6}$ mbar within the detector vessel. Then, the filter knob is adjusted to 124.5°, which puts the 171nm filter underneath the lamp. After, the electrodes are connected to the high-voltage power supply through the pA-meter, whereas the diode is connected to the Keithley electrometer. Once the proper voltages are applied- 5 V to the diode, -350 V to the aperture- the lever on the lid is closed, blocking the light. It takes a couple of minutes for all current values to settle. After that, the software calculates the mean value of the offset for each current, and the recorded values are corrected for the offset. The fields between the electrodes are kept constant, and the current on the diode is measured. This measurement allows the photon rate on the diode, R_{ph}, to be determined with Equation (2.1)

$$R_{ph} = \frac{I_{diode}}{e \cdot QE} \tag{2.1}$$

where e is the electron charge and the QE the quantum efficiency of the diode. At a wavelength of around 161 nm the quantum efficiency of the diode is (8 ± 1) %.

In optical measurements, the solid angle is essential for accurately characterizing light intensity falling on a detector. The solid angle, denoted by Ω, is a measure of the spatial extent of a light source as perceived from a specific point, typically the location of the detector. When performing reference measurements with a diode to determine the photon rate of the active area, correcting for the geometrical factor is crucial to obtaining precise results. The solid angle accounts for the three-dimensional spread of light rays emitted from the source and intercepted by the diode. It is particularly relevant when dealing with non-point light sources or when the light distribution is not uniform, which happens to be the case for the deuterium lamp; see Figure 2.2. The solid angle correction is integral to compensate for variations in the incident angle of light on the detector's active area. Mathematically, the solid angle is defined as the ratio of the subtended area, A, at the center of the sphere to the square of the radius, r:

$$\Omega = \frac{A}{r^2} \tag{2.2}$$

in this case r is the distance to of the diode and the sample. For both cases the distance is (296 ± 4) mm. This means the photon rate on the active are of the sample is given as follows

$$R_{ph}^{PC} = R_{ph} \cdot \frac{\Omega_{PC}}{\Omega_{diode}} \tag{2.3}$$

The ratio between number of electrons released from the photocathode per second, N_e, to the photon rate incident on the photocathode gives the QE for that wavelength. Thus the QE of the photo cathode is given by the following equation:

$$QE = \frac{\frac{I_{meas}}{e}}{R_{ph}^{PC}} = \frac{N_e}{R_{ph}^{PC}}. \tag{2.4}$$

Every uncertainty provided in this bachelor's thesis is calculated with the use of the Gaussian error propagation as described on [54].

2.4.2 Effective Gain in Transmissive Mode

Gain is the ratio between the number of primary electrons and the number of electrons after amplification. However, not all amplified electrons reach the anode; for example, some are collected by the amplification system. Because of this, it is beneficial to introduce effective gain, G_{eff}. The absolute gain considers the total number of amplified electrons, whereas the effective gain only considers the amplified electrons that reach the anode. Therefore, the effective gain could be calculated with the following equation:

$$Gain = \frac{I_{anode}}{I_{primary}} \tag{2.5}$$

where $I_{anode}, I_{primary}$ are the measured current on the anode and the current due to primary electrons.

The system's effective gain depends on the configuration of the potentials applied to the individual layers. Using a source with known properties allows the calculation of the primary current, which means the effective gain of the particular field configuration could be determined by measuring the current on the anode. By using the same configuration in the measurement with the photocathode the primary current can be determined, which cannot me directly measured with the transmissive setup. The direct measurement of the primary current proves challenging due to its exceedingly small magnitude, rendering it beyond the detection capabilities of the pA-meter. Moreover, attempting such measurements faces the additional obstacle of the signal being submerged beneath the inherent noise of the detector.

In order to determine the gain, we used as our source ^{55}Fe isotope, which is known to decay into ^{55}Mn, by capturing electrons, and emits mostly X-rays with an energy of 6 keV [55].

2.4.3 DLC on a Frame

In measuring DLC transparency, the experimental setup involves securing the diode to the sample holder hole and applying a 5-volt voltage to activate the diode. This diode is connected to the pA-meter, where the current on the diode can be measured to determine the intensity of the incident light. The change in intensity is observed by placing the DLC sample between the light source and the diode.

Careful placement of the DLC sample at the center of the sample holder is crucial for measurements because the samples consist of a thin layer of DLC stretched across a frame. The structure of the samples makes them extremely fragile and prone to ripping, so much so that they can tear if they are moved through air too fast. An aperture is positioned on top of the sample holder to ensure consistency. The aperture is also connected to the pA-meter. When the light is incident on the aperture, a positive current is measured, which can be used to gauge the lamp's output. This ensures that the subsequent measurements are comparable, as the comparison is only valid if the lamp's output does not vary significantly. Simultaneously, the DLC sample is placed on the sample holder, aligning it appropriately for the measurements.

The experimental setup involves creating a vacuum and adjusting the filter wheel to position a 171 nm filter underneath the lamp. This specific wavelength is critical for determining the quantum efficiency of DLC at 161 nm. Software calibration follows, wherein the lever on the lid is closed to block light. After a settling period, the software calculates the mean value of the offset for each current, correcting the recorded values.

Current measurements are then conducted using the diode, reflecting changes in light intensity attributed to the presence of the DLC layer. The procedure is repeated for DLC samples with varying thicknesses: empty frame, 3 µm, 4 µm, 6 µm, 8 µm, and 20 µm. After changing each sample, a waiting period is introduced, allowing the vacuum pressure to stabilize before initiating the subsequent measurement. Throughout the experiment, pressure control is maintained at an average of 6.33×10^{-6} mbar.

2.4.4 DLC on Metal

The primary objective of these measurements is to determine the QE of the DLC. In pursuit of this goal, measurements are conducted with coated and uncoated copper samples, providing a comparative analysis of their QE values. Notably, preliminary measurements indicated that the surface finish of the metal affects the QE. To mitigate this impact, all measurements utilize plates that have undergone sand-blasting, as this surface treatment demonstrated the highest QE values in preliminary assessments. This consideration ensures a standardized and optimized approach in evaluating the quantum efficiency of the DLC-coated metal sample.

The DLC-coated metal samples, produced at TUM as previously described, are positioned in the designated slot on the sample holder. A screw is then employed to securely attach a cable, ensuring both the sample and cable are fastened to the sample holder. Following this, the remaining components of the detector are assembled on top of the sample holder, adhering to the configuration described in earlier sections with a gold anode added added underneath the sample holder.

All electrodes and the sample are connected to the pA-meter through the SHV feedthroughs embedded in the wall of the detector vessel. The lid is then sealed, and the experimental setup is allowed to reach a low pressure of approximately 5×10^{-6} mbar.

Voltage is applied to the electrodes in distinct configurations, the names of the respective

Electrode	Current	Voltage
Aperture	$I_{aperture}$	$U_{aperture}$
Mesh	I_{stop}	U_{stop}
Wire plane	I_{wire}	U_{wire}
Sample holder	I_{DLC}	U_{DLC}
Anode	I_{GT}	U_{GT}

Between electrodes	Electric field
Aperture and mesh	E_{suck}
Mesh and wire plane	E_{stop}
Wire plane and sample holder	E_{drift}
Sample holder and anode	E_{ind}

Table 2.2: The variable names; the measured currents and the supplied voltage of each electrode (left). The names of the electric field between the respective electrodes(right).

fields, voltages and currents are shown on Table 2.2. In total, a set of measurements consists of 13 variations. Once the current stabilizes, the light source is activated, and the lamp is allowed to attain optimal operating temperature before measurements begin.

The calibration process, detailed in earlier sections, is executed to ensure accurate readings. This involves closing the lever, initiating a settling period, and calculating the mean offset for each current, correcting recorded values. Then the entire measurement process including the calibration is iterated for each of the 13 distinct configurations.

2.4.5 Transmissive mode

In the transition from the reflective to the transmissive mode, signal amplification becomes crucial as primary electrons alone lack the strength to generate measurable signals. To address this, the detector is filled with a specific gas mixture, Ar-CH_4 (90-10), where methane serves as the quenching gas. The configuration of layers in the transmissive mode differs significantly from the reflective way, as depicted on the right side of Figure 2.5. The details of the setup are as described previously. The amplification with this setup is crucial for detecting and measuring faint, unmeasurable signals.

The amplification process heavily relies on the gas within the detector. Therefore, the flushing procedure is vital for transmissive mode measurements. Firstly, the air within the detector vessel is evacuated using a vacuum pump. Afterward, the detector lid is fixed to the body using six wing nuts. Then, the inlet valve of the detector is open, allowing the flow of Ar-CH_4 at a controlled flow rate of 10 liters per hour. After reaching near atmospheric pressure, the outlet valve of the vessel is opened. This allows the gas to flow through the detector without the outside air flowing back from the outlet valve. A waiting period of at least 15 minutes ensues, ensuring stability of measurements post-flushing. For measurements involving a radioactive source (iron-55), an overnight flush replaces the air due to the source's sensitivity to low pressure.

The measurement procedure for CsI-coated THGEM involves replacing the sample holder with a wire plane and the CsI-coated THGEM in place of the first THGEM. Voltage configurations specified in the first column of Table 2.3 are applied; these values are chosen after a series of measurements to optimize the gain without causing discharges. The gain of the configuration used for this measurement is lower than the other configuration. This is done because the CsI is a better photocathode than DLC; therefore, using the higher gain

Field / Voltage	Low Gain	High Gain
Drift field	$0\,\mathrm{V\,cm^{-1}}$	$0\,\mathrm{V\,cm^{-1}}$
THGEM 1 ΔV	750 V	1000 V
Transfer field	$1800\,\mathrm{V\,cm^{-1}}$	$1800\,\mathrm{V\,cm^{-1}}$
THGEM 2 ΔV	900 V	800 V
Induction field	$2000\,\mathrm{V\,cm^{-1}}$	$2000\,\mathrm{V\,cm^{-1}}$
Ground	0 V	0 V

Table 2.3: Two main voltage configurations used primarily in the thesis. The high gain and low gain are determined experimentally as a result of optimization.

configuration resulted in more frequent discharges. Then, the whole pad plane is scanned, and the measurement order is shown in Figure 2.18. By following a consistent measurement order, we not only standardize the measurement procedure, thus decreasing the variation between measurements, but we also decrease the susceptibility of the measurements to the time-dependent fluctuations of the lamp output.

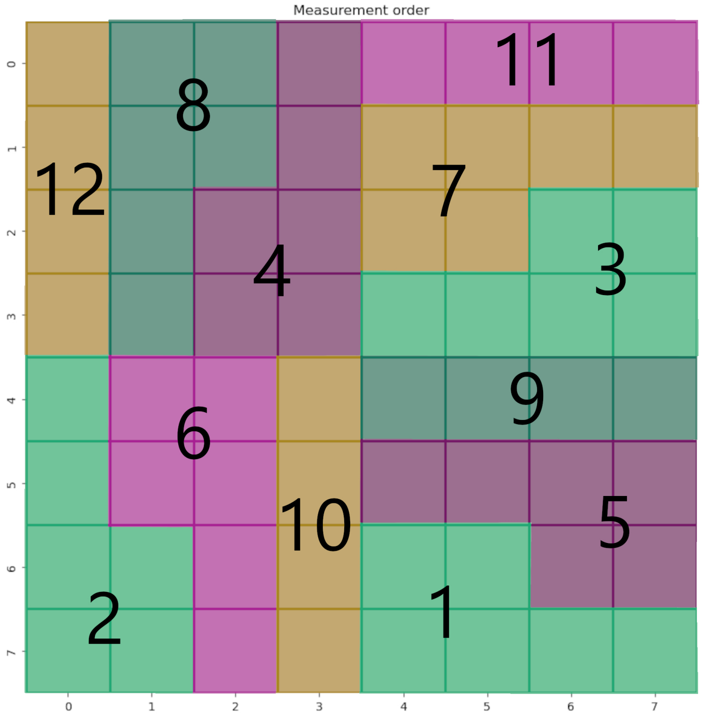

Figure 2.18: Measurement order used during the total scan of the pad plane in the transmissive mode

Moving to measurements withMgF_2 glass coated with DLC, both of the specified voltage configurations in Table 2.3 are applied, and signals from the pads are measured. These measurements followed the depiction on the right side of Figure 2.5. During these measurements, a diode is placed next to the hole of the sample holder. This allows us to accommodate for the fluctuations of the lamp's output. The initial measurements showed that the currents were stabilized after approximately thirty minutes. After the stabilization of the signals, the pads underneath the sample, wherein the DLC layer looks down, are scanned. After this, the sample holder is taken out of the detector, the screws are removed, and the DLC is flipped. Then, the exact measurements are made with the DLC layer looking up. Continuing from the measurements with the flipped DLC-coated sample, the focus shifts to a comparative analysis. By exploring data from both orientations—facing downward and upward—we aim to identify the influence of the transmissive properties of DLC, primarily focusing on the QE of DLC.

3 Results and Discussion

3.1 Transparency of DLC

One fundamental property of a photocathode is its ability to transmit light. The investigation revealed a pronounced dependency on the thickness of the DLC layer. Quantitative measurements demonstrated this correlation, with transparency showing a tangible variation based on DLC thickness. The baseline measurement, conducted with an empty frame, yielded a current reading on the diode of (2.157 ± 0.006) nA. Subsequent measurements with the DLC-coated diode, denoted as $(I_{\mathrm{diode}}$, resulted in a reduced current of $(4.029 \pm 0.080) \times 10^{-2}$ nA. For enhanced clarity, Figure 3.1 illustrates the normalized light transmission normalized to the reference measurement obtained from the empty frame. In Figure 3.1, it should be noted that the error bars associated with the data points are smaller than the size of the data markers. Despite their minimal visibility on the graph, these error bars have been included to represent the precision of the measurements.

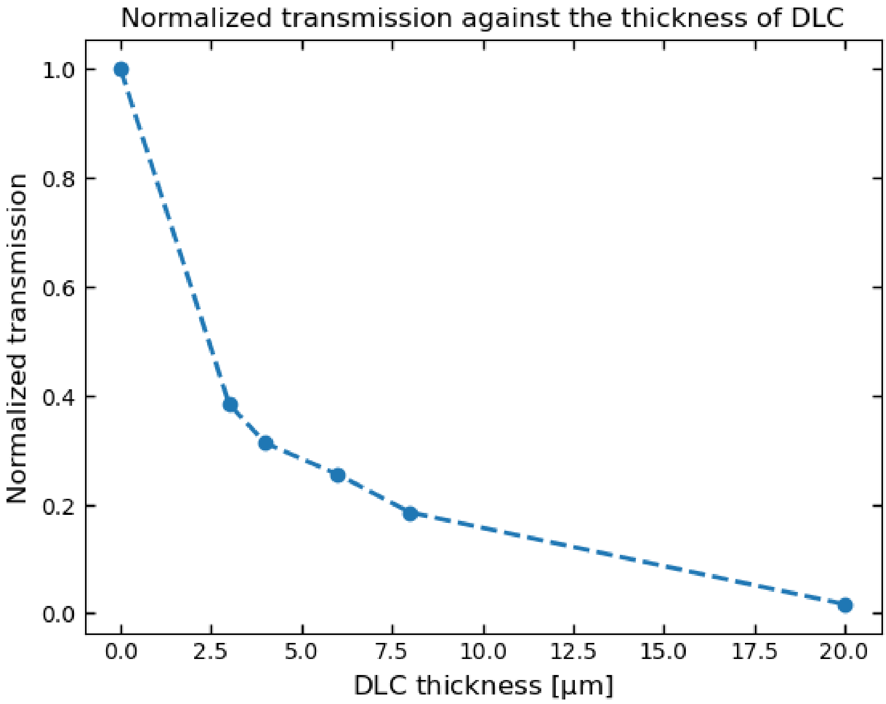

Figure 3.1: Transmission of the DLC with respect to the thickness of the layer. Note that, the error bars are included in the graph but the error bars associated with the data points are smaller than the size of the data markers.

The thicknesses explored ranged from an absent DLC layer of 0 to 20 micrometers. Notably, as the DLC layer thickness increases, there is a consistent decrease in light transmission. This trend is visually evident in the data, with a particularly noteworthy observation at 20 micrometers, where the transmission is measured at 1.69 percent of the reference measurement. The unitless nature of the transmission ratio, ranging from 1 to zero, underscores the progressive reduction in light transmission with increasing DLC thickness. While a precise mathematical trend or best-fit model has not been determined at this stage, the visual representation underscores the inverse relationship between DLC thickness and light transmission. It is worth noting that all known experimental factors have been carefully controlled, enhancing the reliability of these observed trends.

The observed inverse relationship between DLC layer thickness and light transmission carries significant implications for its application as a photocathode, particularly in transmissive mode measurements. The absence of industry standards in this context underscores the pioneering nature of this research, which aims to establish fundamental properties of DLC for use in photocathodes. The practical implication of the trend is crucial for detectors utilizing transmissive mode measurements. As demonstrated, an increase in DLC thickness corresponds to a decrease in light transmission. Therefore, detectors employing transmissive mode measurements should exercise caution in selecting DLC layer thickness for optimal performance. The layer should have a sufficient thickness so that the light interacts with the DLC instead of passing through it. Moreover, in the absence of established standards, this research serves as a foundational step toward defining optimal DLC characteristics for photocathode applications. The lack of predefined thickness ranges emphasizes the pioneering nature of this study, positioning it as a cornerstone in establishing guidelines for DLC implementation in such contexts. While the study does not offer a specific thickness recommendation, it prompts further considerations for the potential use of DLC as an alternative to conventional photocathode materials. Future research exploring variations in DLC layer thickness could provide valuable insights into optimizing performance for specific applications.

3.2 DLC on Copper

Figure 3.2 illustrates the measured currents at each electrode as a function of the increasing electric field E_{drift} in the vacuum conducted with the 171 nm filter. This measurement aims to quantify the number of photoelectrons departing from the photocathode.

When a negative electric field is present between the sample holder and wires, emitted photoelectrons move away from the photocathode toward the wires, resulting in a positive current on the sample, I_{DLC}. This positive current corresponds to the number of emitted photoelectrons. Similarly, the negative current, I_{wire}, at the wires should also reflect the number of emitted photoelectrons. However, this correlation is not exact in a vacuum due to the high velocities that electrons can reach, which can lead them to bypass electrodes without being collected. This phenomenon is particularly evident when comparing I_{DLC} and I_{wire} in Figure 3.2, especially at relatively higher fields. In the low drift field (approximately $-150\,\text{V}\,\text{cm}^{-1}$) region, the absolute values of these two currents align, as expected. Each electron leaving the top side of the sample drifts toward the wires and is detected there as a negative current. Conversely, at high drift fields, the electrons accelerate to velocities that prevent their

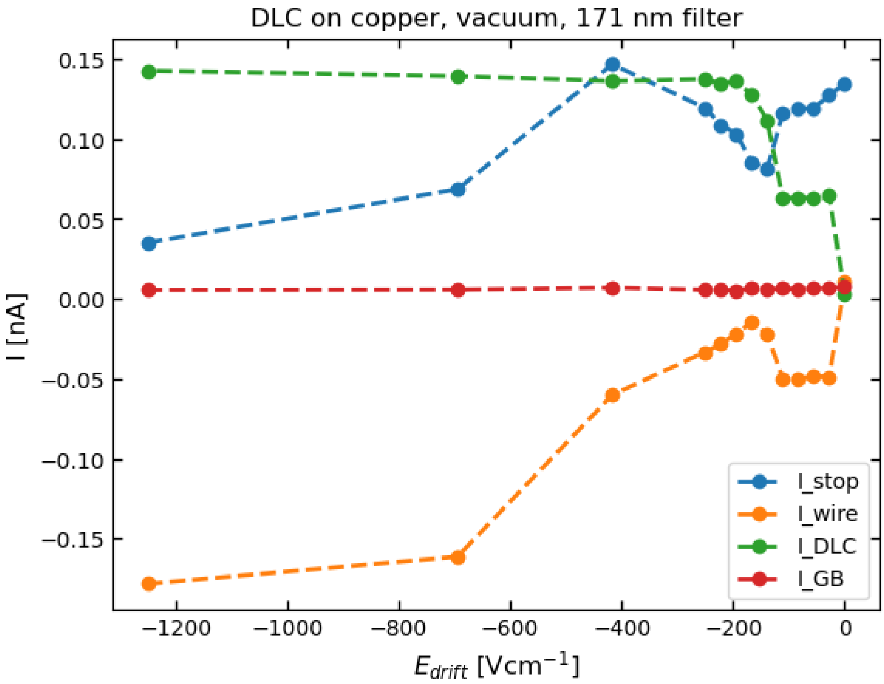

Figure 3.2: Currents at each electrode plotted against the drift field. The measurement are made in vacuum with the 171 nm filter. The sample is the DLC coated copper plate

collection at the wires.

In order to determine the QE of the sample, the plateau region at higher fields is used as the electron ejection saturates. Therefore, it is safe to assume that this region will have the highest QE possible for the sample. The I_{DLC} at the saturated region (0.1395 ± 0.0027) nA. Thus, the QE for DLC and copper combined can be calculated using the previously explained equations. The QE of the DLC and copper combined is determined to be $(1.6 \pm 0.2) \times 10^{-5}$. In the measurements without the coating, the result remained consistent at 1.6×10^{-5}. This parity in measurements led us to conclude that the reflective setup employed in this instance was insufficient for accurately determining the QE of the DLC. In response to this observation, we subsequently implemented a transmissive mode with amplification to enhance the signal.

3.3 Transmissive Mode

Since the measurements with the reflective mode could not determine the QE of the DLC, a switch to the transmissive mode, where the signal is amplified, was necessary. Our initial measurements involved comparing the signals obtained from a CsI-coated THGEM and a non-coated THGEM. By subtracting one from the other, we aimed to determine whether the detector could effectively reveal the impact of the coated region.

However, during the measurements, an unexpected increase in all currents on the active pads and the ground pad surrounding the 64 pads was observed. Despite further investigation, the source of this increase has yet to be determined. Furthermore, the normalization of pad currents to the ground current proved insufficient, as the rate of change is not constant.

It is essential to acknowledge that the current state of our findings renders a quantitative comparison unfeasible. The unforeseen variations in currents and the challenges in normalization prevent us from providing precise quantitative assessments. However, despite these limitations, we have successfully conducted a qualitative comparison, allowing us to discern and analyze broader trends and patterns in the data.

A heat map resulting from the qualitative assessment can be seen on the right side of Figure 3.3 where the difference between the measurements with the coated THGEM and uncoated THGEM is presented. The shape is as expected as the light source can be seen as a point-like radiator emitting light in all directions, and even with the subtraction of background, the effect of CsI coating is observable. The intensity on a point in space is indirectly proportional to the square of the distance from the source. The projection of the coated region can be seen on the left side of Figure 3.3.

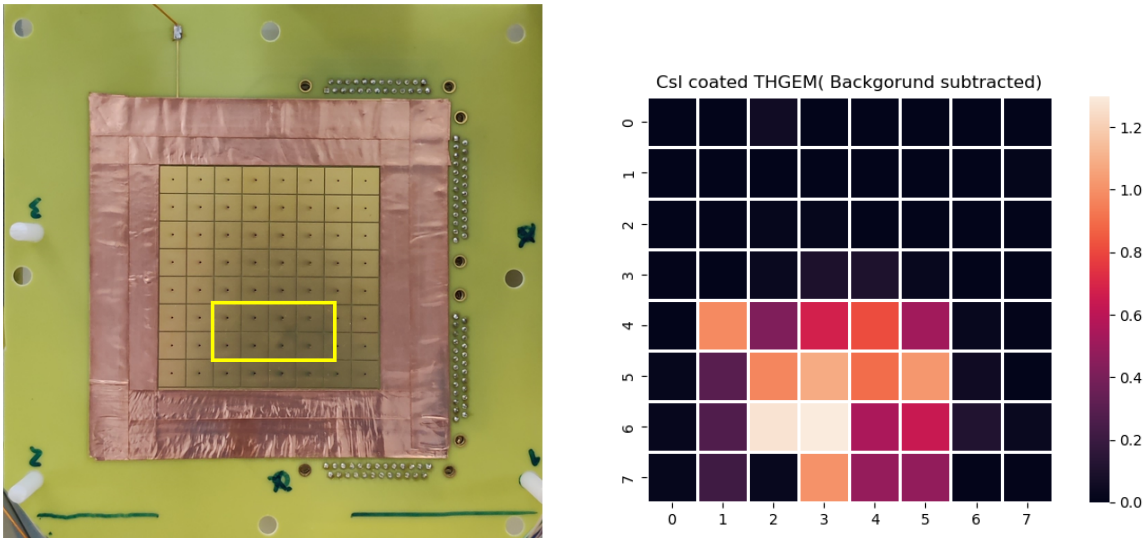

Figure 3.3: The projection of the coated region to the pad plane indicated by the yellow outline (left), heat map of the pad with coated THGEM with subtracted background(right).

Some outlier pads are observed, such as pad A5, see Figure 2.8, where the current is measured despite the activity in the adjacent pads. This lack of signal was not a reoccurring effect as it changed from measurement to measurement. It is currently under investigation due to suspicion of a connection issue in the readout system cabling.

Once we established that the transmissive setup was capable of measuring the difference caused by the photocathode's presence. We switched to measurements using the DLC sample provided by CERN. Figure 3.4 shows the projection of the DLC-coated region on the pad plane.

To enhance clarity and account for the detector's error margin of 0.001, the color scale in the measurement plot shown on the right side of Figure 3.4 begins from 0.002 rather than 0,

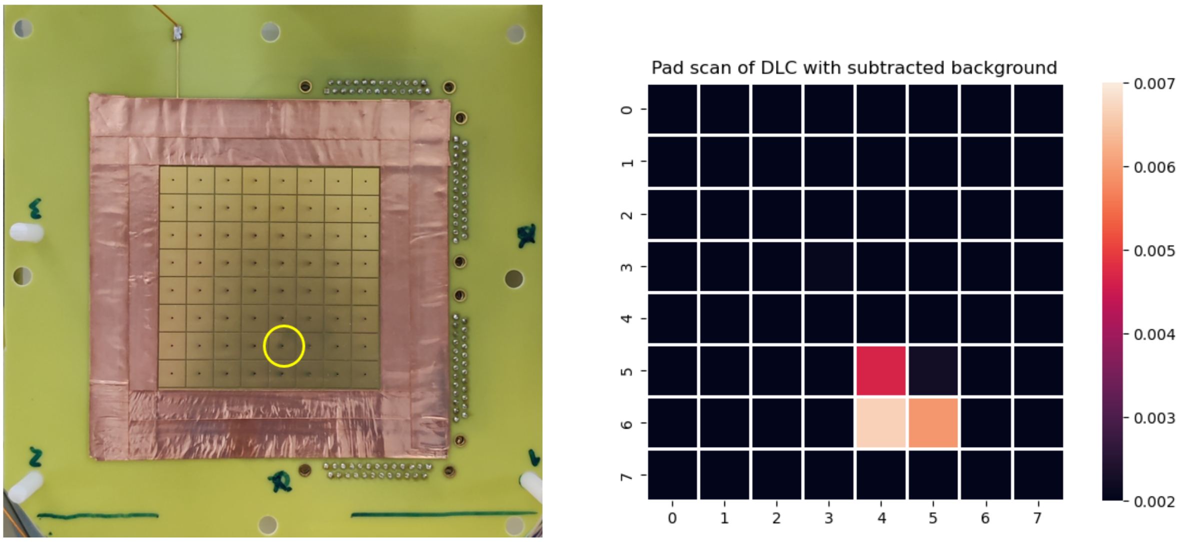

Figure 3.4: Projection of DLC coated region on the pad plane highlighted by the yellow circle(left) and the heat map of the pad current difference between the measurments with DLC looking down and up(right). Note that the scale of the figures are set higher than the measurement precision of the detector.

ensuring a more visually distinct representation of current values on individual pads.

Once again, the region underneath the DLC coating can be distinguished. Following this, the gain of the setup is determined with the ^{55}Fe source. The gain is calculated as (9.84 ± 6.15). Nevertheless, the result is internally consistent. A notable example is the observation of a higher current on the bottom of THGEM 2 before the introduction of the induction field, aligning precisely with the literature since the electron extraction efficiency is less than unity [56]. This internal consistency underscores the reliability of the measurements despite the higher-than-desired error margin. The unusually high error primarily attributed to the limited height of the detector vessel. Due to the setup's dimensional limits, the distance between the source and the first THGEM is less than a centimeter, which decreases the number of electrons generated as result of the sources decay. The minuscule magnitude of the primary current generated by the source contributes significantly to the elevated error in the measurement. Despite the elevated error, efforts were made to capture the data under challenging circumstances, and subsequent analyses should be approached with awareness of this inherent variability.

After determining the gain of the particular configuration, the number of photons illuminating the DLC-coated sample is estimated using Equation (2.3). Then, the primary electron rate is determined by dividing the registered current by the gain of the configuration. Lastly, using Equation (2.4) with these calculated values allows the determination of the QE of DLC in transmissive mode. The QE of the DLC sample is, therefore, estimated to be $(5.93 \pm 3.71) \times 10^{-5}$. Due to the substantial error in the gain measurement, the overall result is also characterized by a significant degree of uncertainty.

Furthermore, we conducted repeated measurements employing various filters shown in Table

2.1; however, the signal generated with the DLC-coated sample proved too faint for accurate measurement. Despite employing different filters to optimize the conditions, the inherent nature of our experimental setup led to a signal that fell below the detectable range. This limitation highlights the challenges associated with measuring extremely low-intensity signals and emphasizes the sensitivity of the detection system to variations in sample properties. Further investigation with filters would require a setup with higher gain.

Throughout the measurements, a notable phenomenon emerged as a temporal evolution in the current on the individual pads. This intriguing behavior is vividly depicted in Figure 3.5, where the currents on the pads exhibit a tangible change over time. The same trend can be observed even when the pad current is corrected with respect to the lamp's output using the diode current. This overarching trend could be an indication of the DLC-coated sample charging up with time and, therefore, changing the electric field around itself.

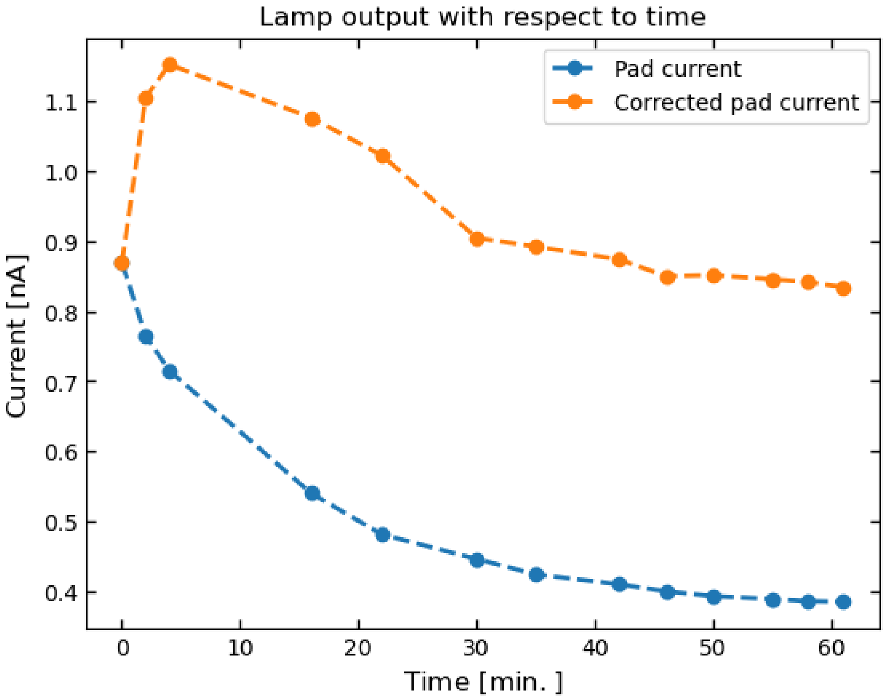

Figure 3.5: Pad current with respect to time, and pad current corrected with respect to the lamp's output using the diode

4 Conclusion

In the course of the thesis, different modes of measurement- reflective mode and transmissive mode- were used in order to investigate the properties of DLC regarding the detection of UV light. The UV transmissivity of DLC with respect to the thickness of the DLC layer is investigated. It was measured that a layer of 20 µm thickness causes the transmission of light to drop to 1.69 %. This suggests that the DLC layer of a detector needs to have sufficient thickness to work efficiently.

Simulations were carried out to examine the behavior of the reflective mode. The paths of ions and electrons within the detector volume have been simulated. This computational analysis served as a confirmation of the system's integrity and functionality. The simulation involved varying field configurations to ensure consistent electron movement toward the readout anode, unaffected by different settings. Furthermore, visualizations of the simulations provided insights into the spatial distribution of particles within the detector, offering a comprehensive understanding of their behavior.

In the reflective mode, copper plates coated with DLC were employed to measure the QE of the DLC. The QE determined for the combination of DLC and copper is $(1.6 \pm 0.2) \times 10^{-5}$, while for copper alone, it is also $(1.6 \pm 0.2) \times 10^{-5}$. Notably, the identical QE values for copper with and without DLC coating suggest that the impact of the DLC coating is not discernible in this measurement configuration.

Then, the measurements were conducted in transmissive mode with the Ar-Ch_4 (90-10) gas mixture. The transmissive mode utilizes a multi-pad anode as the readout anode, which allows the measurement of 64 individual pads. Furthermore, the spatial granularity of the multi-pad anodes allows the distinction between signal and background contribution. The application of CsI-coated THGEM is instrumental in evaluating the detector's ability to distinguish and analyze the influence of a photocathode coating. However, during these measurements, an unexpected increase in the currents on the active pads and ground is observed, which renders a quantitative analysis unfeasible. The reason for this change in currents is currently unknown, and this aspect warrants further investigation to gain a comprehensive understanding. Nevertheless, a qualitative analysis is performed that shows the effect of the coated region.

Subsequently, the gain of the transmissive setup is determined. For this, the primary current generated by an ^{55}Fe is compared to the current on the active readout pads. The gain is calculated as (9.84 ± 6.15). The confined setup limits the distance between the source and the first THGEM, reducing the number of generated electrons. This minimizes the primary current, contributing to a higher measurement error. Acknowledging the limitations of this aspect, further investigation is warranted to enhance the precision of the results.

Lastly, the coated THGEM is replaced by an uncoated one, and the DLC coated MgF_2 is used with the corresponding sample holder. The effect of the DLC coating is observed both qualitatively and quantitatively. The QE of DLC is estimated to be $(5.93 \pm 3.71) \times 10^{-5}$. Due to the substantial error in the gain measurement, the overall result is also characterized by a significant degree of uncertainty.

In summary, the research carried out in the context of this thesis illustrates that the transmissive mode proves effective for investigating the properties of DLC. However, to obtain more precise results, further in-depth investigations are warranted. Additionally, it is noteworthy that the insights gained from this study pave the way for potential applications of DLC in future MPGD-based detectors.

Acknowledgments

I would like to express my deepest gratitude to Berkin Ulukutlu for his unwavering support, guidance, and expertise throughout this research. His valuable insights and encouragement have been instrumental in shaping this work. I am also thankful for the mentorship provided by Dr. Piotr Gasik, whose expertise helped immensely throughout this investigation. Special thanks to Henrik Fribert, Leonardo Bugia and Thomas Klemenz for their collaborative efforts.

This opportunity has not only enhanced my academic knowledge but has also allowed me to work alongside talented colleagues. I am truly thankful for the trust and encouragement provided by Professor Laura Fabbietti throughout my research in the group.

I am grateful to my friends and family for their understanding, encouragement, and patience during this challenging but rewarding journey. Their emotional support sustained me through the highs and lows of the research process.

Finally, I look forward to continuing collaborations and exploring new avenues in future research endeavors.

Thank you to everyone who contributed to the realization of this project.

List of Figures

1.1 Structure of photomultiplier tube with labeled components. Taken from [5] . . . 2
1.2 Cross-section of an avalanche photodiode and its operating principle. Taken from [9] . . . 4
1.3 The generic structure of SiPM cell. Taken from [12] . . . 5
1.4 Energy distribution of molecules and particles at normal conditions. Taken from [15] . . . 8
1.5 Electron drift velocity in argon-methane mixtures at NTP. Taken from [15] . . . 9
1.6 Electric field in the region of the holes of a GEM electrode. Taken from [21] . . . 11
1.7 Schematics of single GEM detector with two-dimensional readout. Taken from [21] . . . 11
1.8 Spectral response curves for various typical photocathode materials. Taken from [31]. . . . 13
1.9 Photoemission described by three-step model. Taken from [35] . . . 14
1.10 Working principle of photodetector with photocathode coated GEM. Taken from [43] . . . 16

2.1 The detector vessel and parts fixed on it. . . . 17
2.2 Technical information of the lamp: Wavelength distribution (left), directivity (middle), and light irradiation range(right). Taken from [44] . . . 18
2.3 Filter wheel removed from the detector vessel lid . . . 19
2.4 General setup used in the experiment . . . 20
2.5 Paths taken by electrons and ions released from the hole of the aperture (left) and above the mesh plane (right). . . . 21
2.6 Wire plane consisting of wires placed across a Kapton frame . . . 22
2.7 A picture of the new Multi-Pad-Anode design on Autodesk Fusion360 (left) and the anode installed in the detector vessel (right) . . . 23
2.8 Modified side panel of the detector vessel (left) and the mapping of the anode(right) . . . 23
2.9 Interior of the coating chamber with an inserted THGEM (left), and a picture taken during the coating procedure where the blue glowing circle is the CsI pill(right). The right side picture is taken from [47] . . . 24
2.10 CsI coating on the THGEM . . . 25
2.11 Glass plate in water (left) and carbon layer on copper in nitric acid (right). Taken from [52] . . . 26
2.12 Different sample holder types: sample holder for metal plates (left), sample holder for the frames (middle), sample holder for glass window (right) . . . 26
2.13 A rendering of the model where the layers are put in their proper order . . . 28
2.14 Example field configuration on COMSOL . . . 28

2.15 Contour of the electric fields within the detectors measurement region in reflective setup . . . 30
2.16 Paths taken by electrons and ions released from the hole of the aperture (left) and above the mesh plane (right). . . . 31
2.17 Path of the electrons released from different heights within the detector. The purple line shows the height from which the electron is released in the simulation. Note that the purple lines are added in photoshop. . . . 32
2.18 Measurement order used during the total scan of the pad plane in the transmissive mode . . . 37

3.1 Transmission of the DLC with respect to the thickness of the layer. Note that, the error bars are included in the graph but the error bars associated with the data points are smaller than the size of the data markers. . . . 39
3.2 Currents at each electrode plotted against the drift field. The measurement are made in vacuum with the 171 nm filter. The sample is the DLC coated copper plate . . . 41
3.3 The projection of the coated region to the pad plane indicated by the yellow outline (left), heat map of the pad with coated THGEM with subtracted background(right). . . . 42
3.4 Projection of DLC coated region on the pad plane highlighted by the yellow circle(left) and the heat map of the pad current difference between the measurments with DLC looking down and up(right). Note that the scale of the figures are set higher than the measurement precision of the detector. . . . 43
3.5 Pad current with respect to time, and pad current corrected with respect to the lamp's output using the diode . . . 44

List of Tables

2.1 Types of filters on the wheel and their position 18
2.2 The variable names; the measured currents and the supplied voltage of each electrode (left). The names of the electric field between the respective electrodes(right). 36
2.3 Two main voltage configurations used primarily in the thesis. The high gain and low gain are determined experimentally as a result of optimization. 37

Bibliography

[1] S. Fukuda, Y. Fukuda, T. Hayakawa, E. Ichihara, M. Ishitsuka, Y. Itow, T. Kajita, J. Kameda, K. Kaneyuki, S. Kasuga, et al. "The super-kamiokande detector". In: *Nuclear Instruments and Methods in Physics Research Section A: Accelerators, Spectrometers, Detectors and Associated Equipment* 501.2-3 (2003), pp. 418–462.

[2] J. Abraham, M. Aglietta, I. Aguirre, M. Albrow, D. Allard, I. Allekotte, P. Allison, J. A. Muniz, M. Do Amaral, M. Ambrosio, et al. "Properties and performance of the prototype instrument for the Pierre Auger Observatory". In: *Nuclear Instruments and Methods in Physics Research Section A: Accelerators, Spectrometers, Detectors and Associated Equipment* 523.1-2 (2004), pp. 50–95.

[3] J. Angle, E. Aprile, F. Arneodo, L. Baudis, A. Bernstein, A. Bolozdynya, P. Brusov, L. Coelho, C. Dahl, L. DeViveiros, et al. "First results from the XENON10 dark matter experiment at the Gran Sasso National Laboratory". In: *Physical Review Letters* 100.2 (2008), p. 021303.

[4] M. Bartolini. "The Upgrade of the LHCb RICH detector". In: *Journal of Physics: Conference Series*. Vol. 2374. 1. IOP Publishing. 2022, p. 012109.

[5] Photonis. URL: `https://psec.uchicago.edu/library/photomultipliers/Photonis_PMT_basics.pdf`.

[6] C. W. Fabjan and H. Schopper. *Particle Physics Reference Library: Volume 2: Detectors for Particles and Radiation*. Vol. 2. Springer Nature, 2020.

[7] N. von SO Flyckt and C. Marmonier. *PHOTOMULTIPLIER TUBES principles & applications*.

[8] L. Collaboration et al. "Lhcb particle identification upgrade technical design report". In: *CERN/LHCC* 22 (2013), p. 2013.

[9] I. I. Izhnin, K. A. Lozovoy, A. P. Kokhanenko, K. I. Khomyakova, R. M. Douhan, V. V. Dirko, A. V. Voitsekhovskii, O. I. Fitsych, and N. Y. Akimenko. "Single-photon avalanche diode detectors based on group IV materials". In: *Applied Nanoscience* (2022), pp. 1–11.

[10] P. Martyniuk, P. Wang, A. Rogalski, Y. Gu, R. Jiang, F. Wang, and W. Hu. "Infrared avalanche photodiodes from bulk to 2D materials". In: *Light: Science & Applications* 12.1 (2023), p. 212.

[11] Y. Liu, X. Yang, R. Wang, and Y. Tang. "Excess noise factor measurement for low-noise high-speed avalanche photodiodes". In: *Physica Scripta* 98.10 (2023), p. 105517.

[12] N. Dinu. "Silicon photomultipliers (SiPM)". In: *Photodetectors*. Elsevier, 2016, pp. 255–294.

[13] O. Bychkova, P. Parygin, E. Garutti, A. Kaminsky, S. Martens, E. Popova, J. Schwandt, and A. Stifutkin. "Radiation hardness study using SiPMs with single-cell readout". In: *Nuclear Instruments and Methods in Physics Research Section A: Accelerators, Spectrometers, Detectors and Associated Equipment* 1031 (2022), p. 166533. ISSN: 0168-9002. DOI: `https://doi.org/10.1016/j.nima.2022.166533`. URL: `https://www.sciencedirect.com/science/article/pii/S0168900222001395`.

[14] E. Engelmann, E. Popova, and S. Vinogradov. "Spatially resolved dark count rate of SiPMs". In: *The European Physical Journal C* 78 (2018), pp. 1–8.

[15] F. Sauli. *Gaseous Radiation Detectors: Fundamentals and Applications*. Cambridge Monographs on Particle Physics, Nuclear Physics and Cosmology. Cambridge University Press, 2023. DOI: `10.1017/9781009291200`.

[16] J. S. Townsend. "The Conductivity produced in Gases by the Motion of Negatively-charged Ions". In: *Nature* 62 (Aug. 1900), p. 340. ISSN: 1476-4687. URL: `https://doi.org/10.1038/062340b0`.

[17] B. Povh, K. Rith, C. Scholz, F. Zetsche, and W. Rodejohann. "Particles and nuclei". In: *An Introduction to the Physical Concepts, Berlin and Heidelberg: Springer-Verlag (Italian Translation:(1998), Particelle e nuclei. Un'introduzione ai concetti sici, Torino: Bollati Boringhieri editore)* (1995).

[18] J. S. Townsend. *Electricity in gases.*, 1915.

[19] H. J. Hilke and W. Riegler. "Gaseous Detectors". In: *Particle Physics Reference Library: Volume 2: Detectors for Particles and Radiation*. Ed. by C. W. Fabjan and H. Schopper. Cham: Springer International Publishing, 2020, pp. 91–136. ISBN: 978-3-030-35318-6. DOI: `10.1007/978-3-030-35318-6_4`. URL: `https://doi.org/10.1007/978-3-030-35318-6_4`.

[20] Y. I. Davydov. "On the first Townsend coefficient at high electric field". In: *IEEE Transactions on Nuclear Science* 53.5 (2006), pp. 2931–2935.

[21] F. Sauli. "The gas electron multiplier (GEM): Operating principles and applications". In: *Nuclear Instruments and Methods in Physics Research Section A: Accelerators, Spectrometers, Detectors and Associated Equipment* 805 (2016), pp. 2–24.

[22] R. Chechik, A. Breskin, C. Shalem, and D. Mörmann. "Thick GEM-like hole multipliers: properties and possible applications". In: *NIM A* 535 (2004), p. 303. ISSN: 0168-9002. URL: `https://doi.org/10.1016/j.nima.2004.07.138`.

[23] A. Breskin, R. Alon, M. Cortesi, R. Chechik, J. Miyamoto, V. Dangendorf, J. Maia, and J. [Santos]. "A concise review on THGEM detectors". In: *NIM A* 598 (2009). Instrumentation for Collding Beam Physics, p. 107. ISSN: 0168-9002. URL: `http://www.sciencedirect.com/science/article/pii/S0168900208012047`.

[24] A. Breskin, M. Cortesi, R. Alon, J. Miyamoto, V. Peskov, G. Bartesaghi, R. Chechik, V. Dangendorf, J. Maia, and J. [Santos]. "The THGEM: A thick robust gaseous electron multiplier for radiation detectors". In: *NIM A* 623 (2010). 1st International Conference on Technology and Instrumentation in Particle Physics, p. 132. ISSN: 0168-9002. URL: `http://www.sciencedirect.com/science/article/pii/S0168900210004390`.

[25] M. Baruzzo, C. Chatterjee, P. Ciliberti, S. Dalla Torre, S. Dasgupta, B. Gobbo, M. Gregori, G. Hamar, S. Levorato, G. Menon, C. Santos, F. Tessarotto, P. Triloki, D. Varga, and Y. Zhao. "Direct measurements of the properties of Thick-GEM reflective photocathodes". In: *Nuclear Instruments and Methods in Physics Research Section A: Accelerators, Spectrometers, Detectors and Associated Equipment* 972 (2020), p. 164099. ISSN: 0168-9002. DOI: `https://doi.org/10.1016/j.nima.2020.164099`. URL: `https://www.sciencedirect.com/science/article/pii/S0168900220305064`.

[26] R. Chechik, M. Cortesi, A. Breskin, D. Vartsky, D. Bar, and V. Dangendorf. "Thick GEM-like (THGEM) detectors and their possible applications". In: *arXiv preprint physics/0606162* (2006).

[27] A. Bondar, A. Buzulutskov, L. Shekhtman, and A. Vasiljev. "Study of ion feedback in multi-GEM structures". In: *Nuclear Instruments and Methods in Physics Research Section A: Accelerators, Spectrometers, Detectors and Associated Equipment* 496.2 (2003), pp. 325–332. ISSN: 0168-9002. DOI: `https://doi.org/10.1016/S0168-9002(02)01763-1`. URL: `https://www.sciencedirect.com/science/article/pii/S0168900202017631`.

[28] F. Sauli. "Progress with the gas electron multiplier". In: *Nuclear Instruments and Methods in Physics Research Section A: Accelerators, Spectrometers, Detectors and Associated Equipment* 522.1-2 (2004), pp. 93–98.

[29] J. Alme, T. Alt, C. Andrei, V. Anguelov, H. Appelshäuser, M. Arslandok, G. Barnaföldi, E. Bartsch, P. Becht, R. Bellwied, et al. "Correction of the baseline fluctuations in the GEM-based ALICE TPC". In: *Journal of Instrumentation* 18.11 (2023), P11021.

[30] D. F. Handbook. *Instrumentation and Control*. 1992.

[31] V. Taillandier. "High speed imaging detectors with diamond dynode materials". PhD thesis. Oct. 2013.

[32] M. S. J. Hashmi. *Comprehensive materials processing*. Newnes, 2014.

[33] A. H. Sommer. "Multi-Alkali Photo Cathodes". In: *IRE Transactions on Nuclear Science* 3.4 (1956), pp. 8–12. DOI: `10.1109/TNS2.1956.4315540`.

[34] A. Burrill, I. Ben-Zvi, T. Rao, D. Pate, Z. Segalov, and D. Dowell. "Multi-Alkali Photocathode Development at Brookhaven National Lab for Application in Superconducting Photoinjectors". In: *Proceedings of the 2005 Particle Accelerator Conference*. 2005, pp. 2672–2674. DOI: `10.1109/PAC.2005.1591224`.

[35] S. O. Flyckt and C. Marmonier. *Photomultiplier tubes: principles and applications; 2nd ed.* Brive: Photonis, 2002. URL: `https://cds.cern.ch/record/712713`.

[36] C. Berglund. *Band Structure and Electron-electron Interactions in Copper and Silver: Photoemission Studies*. 5205. Stanford University, Stanford Electronics Laboratories, Solid-State ..., 1964.

[37] C. N. Berglund and W. E. Spicer. "Photoemission studies of copper and silver: Theory". In: *Physical Review* 136.4A (1964), A1030.

[38] M. Baruzzo, C. Chatterjee, P. Ciliberti, S. Dalla Torre, S. Dasgupta, B. Gobbo, M. Gregori, G. Hamar, S. Levorato, G. Menon, et al. "Direct measurements of the properties of Thick-GEM reflective photocathodes". In: *Nuclear Instruments and Methods in Physics Research Section A: Accelerators, Spectrometers, Detectors and Associated Equipment* 972 (2020), p. 164099.

[39] G. Baishali, V. Radhakrishna, V. Koushal, K. Rakhee, and K. Rajanna. "Study of electron focusing in thick GEM based photon detectors using semitransparent photocathodes". In: *Nuclear Instruments and Methods in Physics Research Section A: Accelerators, Spectrometers, Detectors and Associated Equipment* 729 (2013), pp. 51–57.

[40] M. Alexeev, C. Azevedo, R. Birsa, F. Bradamante, A. Bressan, M. Büchele, M. Chiosso, P. Ciliberti, S. Dalla Torre, S. Dasgupta, et al. "The MPGD-based photon detectors for the upgrade of COMPASS RICH-1". In: *Nuclear Instruments and Methods in Physics Research Section A: Accelerators, Spectrometers, Detectors and Associated Equipment* 876 (2017), pp. 96–100.

[41] J. Agarwala, M. Alexeev, C. Azevedo, F. Bradamante, A. Bressan, M. Büchele, M. Chiosso, C. Chatterjee, A. Cicuttin, P. Ciliberti, et al. "The MPGD-based photon detectors for the upgrade of COMPASS RICH-1 and beyond". In: *Nuclear Instruments and Methods in Physics Research Section A: Accelerators, Spectrometers, Detectors and Associated Equipment* 936 (2019), pp. 416–419.

[42] K. Zeitelhack, A. Elhardt, J. Friese, R. Gernhäuser, J. Homolka, A. Kastenmüller, P. Kienle, H.-J. Körner, P. Maier-Komor, M. Münch, et al. "The hades rich detector". In: *Nuclear Instruments and Methods in Physics Research Section A: Accelerators, Spectrometers, Detectors and Associated Equipment* 433.1-2 (1999), pp. 201–206.

[43] A. Buzulutskov. "Gaseous photodetectors with solid photocathodes". In: *Physics of Particles and nuclei* 39 (2008), pp. 424–453.

[44] Hamamatsu. *Electrostatic charge removers*. May 2023. URL: `https://www.hamamatsu.com/content/dam/hamamatsu-photonics/sites/documents/99_SALES_LIBRARY/etd/VUV_TLSZ1037E.pdf`.

[45] S. Dalla Torre. "Gaseous counters with CsI photocathodes: The COMPASS RICH". In: *Nuclear Instruments and Methods in Physics Research Section A: Accelerators, Spectrometers, Detectors and Associated Equipment* 970 (2020), p. 163768.

[46] L. Bugia. *Characterizing CsI Coated THGEMs for Photon Detection*. 2023. URL: `https://www.das.ktas.ph.tum.de/DasDocs/Public/Bachelor_Theses/BachelorThesis_LeonardoBugia.pdf`.

[47] M. Rieder. *Characterizing CsI Coated THGEMs for Photon Detection*. 2022. URL: `https://www.das.ktas.ph.tum.de/DasDocs/Public/Bachelor_Theses/BachelorThesis_MarkusRieder.pdf`.

[48] J. Friese, R. Gernhäuser, J. Homolka, A. Kastenmüller, P. Maier-Komor, M. Peter, K. Zeitelhack, P. Kienle, and H. Körner. “Enhanced quantum efficiency for CsI grown on a graphite-based substrate coating”. In: *Nuclear Instruments and Methods in Physics Research Section A: Accelerators, Spectrometers, Detectors and Associated Equipment* 438.1 (1999), pp. 86–93. ISSN: 0168-9002. DOI: `https://doi.org/10.1016/S0168-9002(99)00663-4`. URL: `https://www.sciencedirect.com/science/article/pii/S0168900299006634`.

[49] G. Dollinger, P. Maier-Komor, and A. Mitwalsky. “Structure investigations of thin carbon foils”. In: *Nuclear Instruments and Methods in Physics Research Section A: Accelerators, Spectrometers, Detectors and Associated Equipment* 303.1 (1991), pp. 79–87.

[50] G. Dollinger and P. Maier-Komor. “Development of laser plasma ablation-deposition techniques for carbon stripper foils”. In: *Nuclear Instruments and Methods in Physics Research Section A: Accelerators, Spectrometers, Detectors and Associated Equipment* 303.1 (1991), pp. 50–58.

[51] A. Grill. “Diamond-like carbon: state of the art”. In: *Diamond and related materials* 8.2-5 (1999), pp. 428–434.

[52] T. Klemenz. *DLC Surfaces for Photon Detection with THGEMs*. MPGD, Darmstadt Germany. 2022.

[53] CERN. *Garfield++*. 2023. URL: `https://garfieldpp.web.cern.ch/garfieldpp/`.

[54] R. Feynman. “Hinweise zur Beurteilung von Messungen, Messergebnissen und Messunsicherheiten (ABW)”. In: ().

[55] E. Sayre. *THE USE OF LOW ENERGY RADIOACTIVE ISOTOPES IN THE EXAMINATION OF PAINTINGS ON THIN SUPPORTS*. Tech. rep. Brookhaven National Lab.(BNL), Upton, NY (United States), 1964.

[56] C. Azevedo, M. Cortesi, A. Lyashenko, A. Breskin, R. Chechik, J. Miyamoto, V. Peskov, J. Escada, J. Veloso, and J. Dos Santos. “Towards THGEM UV-photon detectors for RICH: on single-photon detection efficiency in Ne/CH4 and Ne/CF4”. In: *Journal of Instrumentation* 5.01 (2010), P01002.